On the use of two-point velocity correlation in wall-pressure models for turbulent flow past a trailing edge under adverse pressure gradient

Jaiswal, Prateek; Moreau, Stéphane; Avallone, Francesco; Ragni, Daniele; Pröbsting, Stefan

DOI
10.1063/5.0021121

Publication date
2020

Document Version
Final published version

Published in
Physics of Fluids

Physics of Fluids

On the use of two-point velocity correlation in wall-pressure models for turbulent flow past a trailing edge under adverse pressure gradient

Cite as: Phys. Fluids **32**, 105105 (2020); https://doi.org/10.1063/5.0021121
Submitted: 07 July 2020 . Accepted: 07 September 2020 . Published Online: 01 October 2020

Prateek Jaiswal, Stéphane Moreau, Francesco Avallone, Daniele Ragni, and Stefan Pröbsting

Physics of Fluids ARTICLE scitation.org/journal/phf

On the use of two-point velocity correlation in wall-pressure models for turbulent flow past a trailing edge under adverse pressure gradient

Cite as: Phys. Fluids 32, 105105 (2020); doi: 10.1063/5.0021121
Submitted: 7 July 2020 • Accepted: 7 September 2020 •
Published Online: 1 October 2020

Prateek Jaiswal,[1,a] Stéphane Moreau,[1,b] Francesco Avallone,[2,c] Daniele Ragni,[2,c] and Stefan Pröbsting[2,3,d]

AFFILIATIONS

[1] Department of Mechanical Engineering, University of Sherbrooke, Sherbrooke, Quebec J1K 2R1, Canada
[2] Faculty of Aerospace Engineering, Delft University of Technology, Delft 2629HS, The Netherlands
[3] Department of Naval Architecture and Ocean Engineering, Shanghai Jiao Tong University, Shanghai 200240, China

[a] **Electronic mail:** prateek.jaiswal@usherbrooke.ca
[b] **Author to whom correspondence should be addressed:** stephane.smoreau@gmail.com
[c] **URL:** https://www.tudelft.nl/en/ae/
[d] **URL:** http://en.sjtu.edu.cn/academics/schools/the-school-of-naval-architecture-ocean-and-civil-engineering/

ABSTRACT

Two-point velocity statistics near the trailing edge of a controlled diffusion airfoil are obtained, both experimentally and analytically, by decomposing Poisson's equation for pressure into the mean-shear (MS) and turbulence–turbulence (TT) interaction terms. The study focuses on the modeling of each interaction term, in order to allow for the reconstruction of the wall-pressure spectra from tomographic velocimetry data, without numerically solving for pressure. The two-point correlation of the wall-normal velocity that describes the magnitude of the MS source term is found to be influenced by various competing factors such as blocking, mean-shear, and the adverse mean pressure gradient. The blocking term is found to supersede the other interaction terms close to the wall, making the two-point velocity correlation self-similar. The most dominant TT term that contributes to far-field noise for an observer located perpendicular to the airfoil chord at the mid-span is shown to be the one that quantifies the variation of the wall-normal velocity fluctuations in the longitudinal direction because of the statistical homogeneity of turbulence in planes parallel to the wall. A model to determine the contribution of the TT interaction term is proposed where the fourth-order two-point correlation can be modeled using Lighthill's approximation. However, its contribution toward wall-pressure spectra is found to be substantially lower than the MS term in the present case.

NOMENCLATURE

C	airfoil chord
$C_{ij,kl}$	fourth-order two-point zero time delay correlation
C_p	mean pressure coefficient
H	boundary layer shape factor
$\boldsymbol{k}$	(k_1, k_3), wall-parallel wavenumber vector
k	$\sqrt{k_1^2 + k_3^2}$, wall-parallel wavenumber vector magnitude
k_1, k_2, k_3	aerodynamic wavenumbers
K_v	modified Bessel function of the second kind of order v
l_y	generalized correlation length
p'	fluctuating wall-pressure
p_{rms}	root-mean-square of the wall pressure
Q_∞	inlet free stream dynamic pressure
Re_c	Reynolds number based on the chord
R_{ij}	second order two-point zero time delay correlation

S_{ij}	single sided velocity wavenumber cross-power spectral density
TT_{ij}	second-order velocity tensor
U_1, U_2, U_3	mean velocity in the trailing edge reference frame
u_1', u_2', u_3'	turbulent velocity in the trailing edge reference frame
U_∞	inlet velocity
U_c	convective speed of wall-pressure fluctuations
U_e	boundary layer edge velocity
V_x, V_y	mean velocity in the wind tunnel reference frame
x, y, z	wind tunnel coordinate system
x_1, x_2, x_3	coordinate system aligned with the trailing edge
α, β, γ	anisotropic stretching parameters
α_g	geometric angle of attack
β_c	Clauser's parameter
$\Gamma(\nu)$	gamma function
δ^*	boundary layer displacement thickness
δ_{95}	boundary layer thickness based on 95% of U_e
θ	boundary layer momentum thickness
$\Lambda_{ij}^{k\pm}$	integral length scale of velocity
$\Pi(f)$	single sided wall-pressure frequency auto-power spectral density
$\Pi(k_1)$	single sided wall-pressure wavenumber auto-power spectral density
Π_c	Cole's wake strength parameter
$-\rho\overline{u_1 u_2}_{max}$	maximum Reynolds shear stress
ρ_∞	incoming air density
τ	integral time scale of turbulence

I. INTRODUCTION

Modeling the pressure field induced by the turbulent velocity field in a boundary layer is essential in many engineering applications including airfoil or blade self-noise, structural vibration and noise radiation, and aerodynamic losses and instability (flutter). In airfoil self-noise, the high-frequency model by Amiet (1976), or its extension to lower frequencies by accounting for the finite chord length [see Roger and Moreau (2005), for instance], directly relates the far-field acoustic pressure to the wall-pressure statistics near the trailing edge. Such models have been successfully validated by Moreau and Roger (2005, 2009) and Roger and Moreau (2004) by performing a set of dedicated experiments on several airfoils including a Controlled-Diffusion (CD) airfoil. The latter is an airfoil type for which the drag is reduced by controlled diffusion or growth of the boundary layer, which has recently been used in many modern turbomachinery applications including compressors, contra-rotating open rotors, turbofans, and ventilation systems. However, modeling the wall-pressure fluctuations is particularly challenging not only because of its arduous mathematical description but also because of the abstruse nature and scarcity of data on the two-point velocity statistics that dictate them. The present state of wall-pressure modeling can be encapsulated in the words of Chase (1980) who said some 40 years ago "Attainment of a comprehensive, validated, satisfactory description of the pressure fluctuations on a wall bounding turbulent flow, despite progress over a protracted period, remains elusive."

Wall-pressure fluctuations either can be directly measured using remote microphone probes (RMPs) or can be determined from velocity measurements using Particle Image Velocimetry (PIV) data, provided that Poisson's equation for pressure is numerically solved [see De-Kat and Van-Oudheusden (2012), Ghaemi *et al.* (2012), and Schneiders *et al.* (2018), for instance]. Computationally, the surface pressure field can be obtained by performing Direct Numerical Simulations (DNSs) [see Abe (2017), Choi and Moin (1990), Na and Moin (1998), Sandberg and Jones (2011), and Sanjosé *et al.* (2011), for instance] that resolve all turbulent scales in the flow or Large Eddy Simulations (LESs) that only resolve the relevant, larger scales [see Christophe and Moreau (2008), Wang *et al.* (2009), and Winkler and Moreau (2008), for instance]. In all cases, these methods are complex, time-consuming and can hardly be used for engineering purposes. For design optimizations, analytical models should be preferred. In the past, several such approaches including either statistical [see Grasso *et al.* (2019), Hodgson (1962), Panton and Linebarger (1974), Parchen (1998), Remmler *et al.* (2010), and Slama *et al.* (2018), for instance] or semi-empirical methods [see Hu (2018), Lee (2018), and Rozenberg *et al.* (2012), for instance] have been used to reconstruct wall-pressure spectra. While the statistical methods describe the non-local velocity fluctuations using two-point velocity correlation, the semi-empirical models rely on finding suitable integral boundary layer parameters to describe non-local flow events. For example, Rozenberg *et al.* (2012) used integral boundary layer scales such as Coles's parameter Π_c (Coles, 1956) to account for the boundary layer history. The semi-empirical models also rely on finding suitable boundary layer parameters to scale the wall-pressure spectra. However, a universal scaling of pressure spectra can only be obtained for a narrow range of frequencies using either inner or outer scales exclusively [see p. 362 of Camussi (2013)]. Semi-empirical models are therefore calibrated using inner and outer boundary-layer variables for various test cases. For instance, Rozenberg *et al.* (2012) used the velocity flow field information at the trailing edge of the CD airfoil at 8° and 16 m/s as one of the test cases for calibration. Although Rozenberg's model is fairly well-tuned and succeeds in capturing the trend and magnitude of the wall-pressure spectra [see Hu (2018), Lee (2018), and Morilhat *et al.* (2019)], it relies on pre-established scaling laws that are not universal.

The statistical approach follows Kraichnan (1956) methodology and splits the source in two partial pressure terms: the mean-shear (MS) term and the turbulence–turbulence (TT) term [see Grasso *et al.* (2019), Panton and Linebarger (1974), Parchen (1998), Remmler *et al.* (2010), and Slama *et al.* (2018), for instance]. Even in this case, assumptions such as turbulent flow homogeneity are used to simplify wall-pressure spectra calculations. For example, Slama *et al.* (2018) and Chase (1980) assumed homogeneous turbulence in all three directions, while Panton and Linebarger (1974) and Remmler *et al.* (2010) made an assumption of turbulence homogeneity on a plane parallel to a wall. The hypothesis of turbulence homogeneity for a flow past an airfoil has nevertheless been questioned in the past [see Albarracin *et al.* (2012), for instance]. Hence, the first objective of the current paper is to assess the validity of the assumption of homogeneous turbulence in the presence of mean adverse pressure gradient and its impact on the modeling of the two-point correlation.

For the flow past an airfoil, another important aspect is to quantify the role of a solid wall on the two-point velocity correlation. In the past, several researchers [see Hunt *et al.* (1987), for

instance] have shown that the wall-normal velocity correlation is strongly affected by the phenomenon of "blocking," especially at a high Reynolds number and in the absence of a mean pressure gradient. Hunt *et al.* (1987) found that the wall-normal velocity correlation profiles between two eddies in the wall-normal direction become self-similar when plotted as a function of the ratio between distances of the eddies from the wall. The existence of self-similarity of the two-point correlation was later demonstrated analytically by Oberlack (2001). Therefore, blocking clearly plays a critical role in defining the extent of the two-point correlation in the wall-normal direction and thereby also controlling the MS term. However, this effect has not been accounted for in the previous studies [see Parchen (1998), Slama *et al.* (2018), and Stalnov *et al.* (2016), for instance] that use an isotropic turbulence model. Moreover, the study of Hunt *et al.* (1987) among others was done for zero mean pressure gradient, and therefore, the role of the pressure gradient on two-point velocity correlation is unclear. The second objective of the present paper is therefore to assess the competing effects of the streamwise mean pressure gradient and the crosswise variation of the mean shear induced by the airfoil surface and to quantify the effect of wall blocking on the two-point velocity correlation in the presence of a mean pressure gradient.

Another aspect of the two-point correlation model lies in the determination of the correlation length. This has been done in the past using semi-empirical laws. For example, Panton and Linebarger (1974) proposed an empirical model based on fitting data of the correlation length of the wall-normal velocity component measurements of Grant (1958). Remmler *et al.* (2010), Kamruzzaman *et al.* (2011), and more recently, Stalnov *et al.* (2016) have employed Prandtl's mixing layer theory to estimate this length. However, Grasso *et al.* (2019) showed that the correlation length might be significantly underestimated by this theory. In fact, there are few experimental and numerical data to assess the validity of this model in estimating the wall-normal correlation length of the wall-normal velocity. Moreover, the mixing length theory does not incorporate the effect of blocking. Therefore, our third objective is to test the previously proposed models of correlation length against our experimental data.

Finally, the relative contribution toward surface pressure fluctuations by individual terms, i.e., the mean-shear (MS) term and the turbulence–turbulence (TT) interaction, has long been a matter of debate. Approximations by early researchers such as Kraichnan (1956) and Hodgson (1962) showed that the contribution of the TT term is small when compared to the MS term. This was later challenged by Chase (1980), Kim (1989), and Chang (1998). Nevertheless, the models proposed by Panton and Linebarger (1974) and Remmler *et al.* (2010), and the TNO-Blake model (Blake, 2017; Parchen, 1998; and Stalnov *et al.*, 2016) all neglect the contribution of the TT term, but they are still able to predict the overall shape and magnitude of the wall-pressure spectra with reasonable accuracy. Therefore, the relative importance of these terms seems to depend on the flow conditions. Alternatively, their models may have overestimated the contribution of the MS term. It is therefore important to assess the contribution of either of these terms. The modeling of the TT source term is inherently more complex since it requires determination of higher order statistics [as shown by Grasso *et al.* (2019)]. In order to simplify the representation and computation with lower order statistics, a hypothesis of normal distribution was first proposed by Millionshchikov (1941). This assumption has been extensively used by Hodgson (1962), Slama *et al.* (2018), and Grasso *et al.* (2019) in the past. However, this was done based on very limited experimental evidence and the assumption was made based on measurements done in a free shear layer only [see Mahinder (1953) and Stewart (1951), for instance]. Many recent studies have shown that the normal distribution assumption does not hold for a wall-bounded channel flow in the absence of a pressure gradient [see Chang (1998), Kim (1989), and Srinath (2017), for instance]. Therefore, this assumption needs to be validated in a realistic flow field with a mean pressure gradient.

The fourth objective is to determine the relative importance of individual source terms of TT and to compare the relative contribution of the MS and the most dominant TT terms. The accuracy of the final result will be gauged against the measured wall-pressure spectra. As a final objective, the regions within the boundary-layer that contribute to the wall-pressure spectra are examined for a given range of frequency, as was done for turbulent channel flows by Abe *et al.* (2005) or more recently by Anantharamu and Mahesh (2020). This helps understand how the non-local velocity fluctuations drive the wall-pressure fluctuations.

To achieve the aforementioned objectives, a well resolved flowfield (at least in space) is of paramount importance. Moreover, long enough signals are necessary to yield reliable high-order statistical quantities such as two-point correlations. Only few previous experiments [see Gavin (2002), Grant (1958), Kamruzzaman *et al.* (2011), Krogstad and Skåre (1995),and Townsend (1980), for example] have looked in details at two-point velocity correlations. They all used Hot Wire Anemometry (HWA), which provided the proper time resolution but was intrusive in nature. Numerically, the two-point velocity correlation has also been studied by Hunt *et al.* (1987), Zawadzki *et al.* (1996), and Sillero *et al.* (2014) but limited to the flow over a flat plate without any mean pressure gradient. In the present study, Particle Image Velocimetry (PIV) has therefore been used to measure the velocity field around the CD airfoil, for which various mean pressure gradients occur on its suction side. The latter has also been chosen as a large set of numerical and experimental data exists on this airfoil [see Boukharfane *et al.* (2019), Moreau *et al.* (2003; 2006; 2016), Neal (2010), Roger and Moreau (2004), Sanjosé *et al.* (2011), and Wu *et al.* (2018), for instance].

II. EXPERIMENTAL SETUP AND INSTRUMENTATION

The aforementioned Controlled Diffusion (CD) airfoil has a 0.1347 m chord, 0.3 m span, 4% thickness-to-chord ratio, and 12° camber angle. For the results to be comparable with the previous studies of Neal (2010), Sanjosé *et al.* (2011), and Wu *et al.* (2018), this airfoil is placed in the jet potential core of an open-jet tunnel at a geometric angle of attack of $\alpha_g = 8°$, and the Reynolds number based on chord Re_c is equal to 1.5×10^5. To reproduce the correct loading, the same jet width of 50 cm [based on the findings of Moreau *et al.* (2003 and 2006) is used in two experiments carried out in the A-Tunnel at the Technical University of Delft (TU Delft). During the first experiment, planar measurements have been carried out in the boundary layer close to the trailing edge on the airfoil suction side and in the near wake. In the second experiment, Time-Resolved Tomographic PIV (TR-Tomo PIV) measurements near the trailing edge were performed.

The A-Tunnel at Delft is an open-jet facility that has been recently refurbished to anechoic. It has a circular opening with a cross section of 60 cm. The free-stream turbulence intensity at the exit of the circular section of the jet was reported to be equal to 0.02% [see p. 78 of Ghaemi (2013)]. To mount the CD airfoil and to compare with previous experimental and numerical setups, two other sections were mounted on top of the original circular test section. The final open-jet nozzle exit was made rectangular with an outlet section of 50 × 30 cm^2. The airfoil is placed between two laser-cut side plates to give the airfoil the prescribed geometrical angle of attack. The machining accuracy of the laser cut is less than 0.125 mm. The laser-cut section is located in the middle of the side plates, which ensures the airfoil to be placed at the center of the nozzle exit. The side plates are made from plexiglass and are 4.76 mm thick to provide good optical access for the PIV measurements.

A. Wall-pressure measurements

To determine the mean loading coefficient, several pinholes are located along the chord and span, as shown in Fig. 1. The diameter d of these orifices is equal to 0.5 mm each. They allow the measurement of pressure fluctuations using Remote Microphone Probes (RMPs) [see Moreau and Roger (2005), for instance] and static pressure sensors [see Neal (2010), for instance]. To measure the mean pressure coefficient, C_p, a PSI System 8400 equipped with ESP pressure scanners was used. These scanners have a range of ±0.36 psi with an accuracy of ±0.03% in the full scale pressure range. For the measurement of pressure fluctuations, RMPs were calibrated *in situ* by applying white noise via a loudspeaker, which was recorded as the output of a NI 9263 audio card. A pre-calibrated microphone was placed in front of and close to the pinhole of the RMP. The reference microphone and RMP signals were recorded simultaneously for 30 s. Coherence levels were checked between the reference signal and RMP and were found to be higher than 95%. The slight loss in coherence results in uncertainty that can be approximated according to Bendat and Piersol (2011) by

$$\epsilon = \sqrt{2}\frac{1-\Gamma^2}{\Gamma\sqrt{N_s}}, \tag{1}$$

where N_s is the number of sets, which in this case is equal to 120, and Γ^2 is the squared coherence magnitude. The total uncertainty encountered due to finite coherence in calibration of RMPs is estimated to be equal to ±0.03 dB (based on the percentage of reference pressure defined as 2×10^{-5} Pa). Finally, a transfer function can be built, which can account for the loss of amplitude and phase,

$$H(f) = E\left[\frac{G_{yy}}{G_{xx}}\right], \tag{2}$$

where $H(f)$ is the attenuation function, E is the expected value, G_{yy} is the auto-spectrum of the reference microphone signal, and, finally, G_{xx} is the auto-spectrum of the RMP measurement. Each measured spectrum is then multiplied by this attenuation function $H(f)$ to yield the single point spectra reported below. The final auto-spectra are calculated by dividing the signals into blocks of size equal to 1 s with an overlap of 75%, resulting in 120 sets in total. The uncertainty in calculating the auto-spectra can be estimated using the following equation outlined by Bendat and Piersol (2011):

$$\epsilon = \frac{2}{\sqrt{N_s}}. \tag{3}$$

Thus, the uncertainty was found to be equal to 0.7 dB. Another important aspect that yields measurement uncertainty at high frequencies is caused by the finite size of the microphone sensors [see Gravante *et al.* (1998), for instance]. In our case, it scales with the diameter of the pinholes. However, it was recently shown by Grasso *et al.* (2019) that this attenuation occurs at very high frequencies around 30 kHz–40 kHz. This occurs well beyond the range of frequencies of interest, and hence, no corrections on higher frequency will be done in the present study.

B. Velocity measurements

Velocity measurements around the CD airfoil were obtained with PIV. Four different sets of planar-PIV measurements were performed using a single LaVision Imager LX 16M CCD 16 megapixel camera with a pixel pitch of 7.4 μm and an EverGreen 200 mJ ND:YAG laser, as shown in Fig. 2, during the first measurement

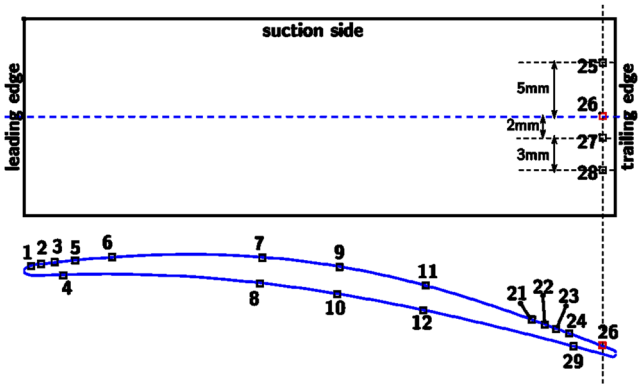

FIG. 1. Location of pinholes on the CD airfoil.

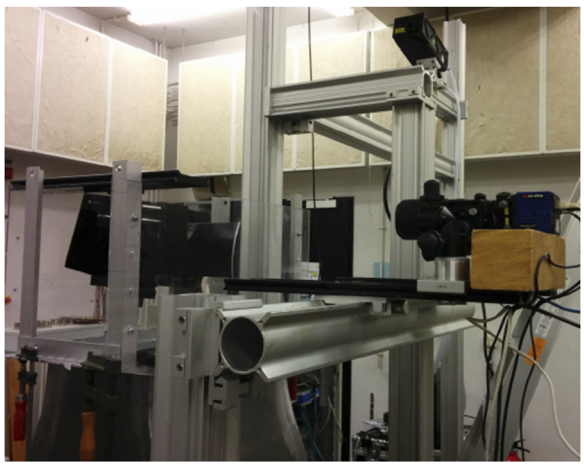

FIG. 2. Planar-PIV setup.

TABLE I. Parameters used for planar-PIV measurements.

Parameters	M1 suction-side boundary layer	M2 pressure-side	M3 suction-side	M4 wake
Depth of focus (mm)	~1.4	~8.5	~6	~2.5
Number of images	2050	2000	2700	2300
Interrogation window (pixel^2)	24 × 24	16 × 16	16 × 16	16 × 16
Lens focal length (mm)	200	105	105	200
FOV (mm^2)	48	~174	~141	~76
Particle image diameter (pixel)	~4	~2.3	~2.43	~2.8
Magnification	0.756	0.215	0.26	0.486
Digital magnification (mm/pixel)	100	27.58	34.04	63.15
Maximum particle image displacement (pixel)	16	17	16	15
Acquisition frequency (Hz)	0.5	0.5	0.5	0.5

campaign. The laser-sheet thickness was measured to be less than 1.3 mm. About 2000 images in a double frame were recorded for all the cases. The camera was fitted with an AF Nikkor 200 mm 1:4 D lenses for near-wake and suction-side boundary-layer measurements, while the velocity contours on the pressure and suction sides were obtained using a 105 mm Nikkor lens. The images were obtained with an acquisition frequency of 0.5 Hz. The parameters used for the PIV measurements are summarized in Table I.

During the second campaign, time-resolved tomographic PIV was employed, using four FASTCAM SA1.1 1 megapixel cameras and a high speed ND-YLF laser. The cameras were placed as shown in Fig. 3. The parameters used for the tomographic PIV are listed in Table II.

Based on the previous computational and experimental studies on the CD airfoil at the same flow condition, the boundary-layer thickness at RMP 26 (98% chord) was estimated to be equal to about 5 mm–6 mm [see Table III of Christophe *et al.* (2015)]. For this reason, the suction-side boundary-layer measurements were carried out with a higher resolution setup. The camera was tilted in such a way that velocities obtained were in the wall-normal direction.

For both setups, glycerin particles were used for seeding, and the particle size was about 1 μm.

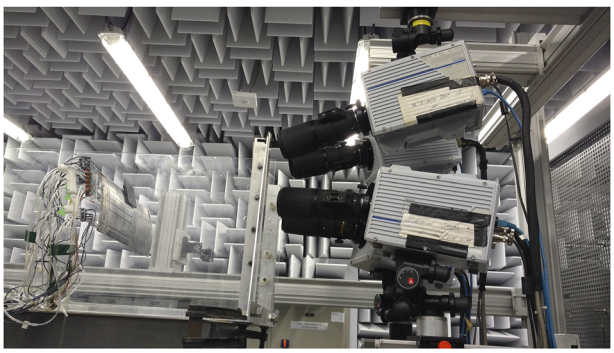

FIG. 3. Tomo-TR PIV setup.

C. Image processing and data reduction of planar-PIV data

Planar-PIV data were processed using Davis 8.1.4 software from LaVision. The images were first pre-processed to reduce the background noise by using the subtract minimum filter. The vector fields were computed by a multi-grid cross-correlation scheme, with a final window size of 16 × 16 pixels^2 except for the case of the suction-side boundary-layer for which the window size was increased to 24 × 24 pixels^2 (due to relatively lower particle density). An elliptical weighting window (with a weighting ratio of 2:1) was used to improve the signal-to-noise ratio of the cross correlation. Dual frame cross correlation was used to compute the vector field. Outliers were detected using the universal outlier detection method of Westerweel and Scarano (2005). The values of vector removal and insertion were chosen to be equal to the ones recommended by Westerweel and Scarano (2005).

The random error for PIV is estimated to be in the order of 0.1 pixel for the algorithm used to map the correlation peak. With this value, the relative error in velocity measurements is 0.67% of the free-stream velocity, as shown in Table I. The uncertainty in calculating mean and standard deviation of velocity scales inversely with the number of independent samples and with the square root of the number of independent samples, respectively [see p. 279 of

TABLE II. Parameters used for Tomo-PIV measurements.

Parameters	Values
Volume size (cm^3)	4 × 2 × 0.5
Number of images	2816
Voxel size (pixel^3)	24 × 24 × 24
Lens focal length (mm)	200
Numerical aperture *F#*	11
Magnification	0.58
Maximum particle image displacement (pixels)	20
Acquisition frequency (kHz)	3.0

TABLE III. Uncertainty quantification for various measured quantities.

Quantity measured	Uncertainty (95% confidence)
Tunnel inlet velocity	1% U_∞
Dynamic pressure	0.5% Q_∞
Random error mean velocity (planar-PIV)	0.67% U_∞
Random error mean velocity (Tomo-PIV)	0.1% U_∞
Averaging uncertainty ${u_i}'$ (planar-PIV)	3.1% $\sqrt{{u_i}'}$
Averaging uncertainty ${u_i}'$ (Tomo-PIV)	4.5% $\sqrt{{u_i}'}$
Averaging uncertainty $R_{ij} = 0.05$ (planar-PIV)	4.5%
Averaging uncertainty $R_{ij} = 0.05$ (tomo-PIV)	5.7%
Averaging uncertainty $\Lambda_{ij}^{k\pm}$ (planar-PIV)	1% $\Lambda_{ij}^{k\pm}$
Averaging uncertainty S_{22}^{1} (planar-PIV)	4.4%
Averaging uncertainty $\frac{{u_i}'^4}{({u_i}'^2)^2}$ (planar-PIV)	43% ${u_i}'^2$

Glegg and Devenport (2007)]. The uncertainty in mean and standard deviation for planar-PIV measurements is thus quantified and shown in Table III. U_∞ and ρ_∞ stand for the free-stream velocity and density at the nozzle exit, respectively. $Q_\infty = 0.5\rho_\infty U_\infty^2$ is the corresponding dynamic pressure. ${u_i}'$ are the rms velocity components in a local Cartesian reference frame attached to the airfoil surface at the considered RMP. R_{ij} and S_{ij}^i are velocity correlation or power-spectral-density tensors, respectively. In all local tensors, the indices are $i, j = 1, 2, 3$, with (1) the wall-tangential, (2) the wall-normal, and (3) the transverse directions.

D. Image processing and data reduction for Tomo-PIV data

The data were processed using Davis 8.4 software from LaVision. The fast-MART algorithm was used for volume reconstruction. For the processing, 10 SMART [see Atkinson and Soria (2009), for instance] iterations with nine smoothing operations were performed. Finally, direct correlation was used to get the three-dimensional velocity profile. Here, the multigrid scheme was used as in the case of planar-PIV, starting with a coarse grid of size 80 × 80 × 80 pixels^3 to all the way down to 24 × 24 × 24 pixels^3. A universal outlier detection scheme was used to detect and replace outlier vectors. The uncertainty in the TR-Tomo PIV measurements was obtained by considering both the random and systematic errors. Ghaemi *et al.* (2012) estimated the random error ϵ_u as

$$\epsilon_u = 0.2\, vxl \frac{1}{S\Delta t}, \tag{4}$$

where S stands for the digital magnification, vxl stands for the voxel size, and Δt stands for the time between two image pairs. Finally, various sources of error in all the measured quantities are summarized in Table III.

III. VALIDATION OF THE FLOW FIELD

A. Mean airfoil loading

To make sure that the flow qualities do not play a significant role when comparing the results in the two different experimental campaigns, the mean wall-pressure coefficient has first been compared. The results in four different facilities, which the CD airfoil has been tested in within a 50 cm jet, show an overall good agreement over most of the airfoil chord, c, as shown in Fig. 4. (x, y) represents the fixed laboratory reference frame at the airfoil mid-span, x being parallel to the jet axis and oriented with the flow. The error bars in the different measurements are within the size of the symbols and mostly concentrated at the leading edge, as shown in Moreau *et al.* (2003) (Fig. 2), for instance.

However, small discrepancies are visible near the plateau in the leading-edge region and can be attributed to the size of the laminar re-circulation bubble. The latter affects the exact location where the boundary layer transition from laminar to turbulent flow starts. The reason for the discrepancies is that the location of the laminar separation bubble is dependent on the inlet free-stream turbulence intensity that varies between the wind tunnels and the numerical simulations [see McAuliffe and Yaras (2010), for instance].

B. Flow field description

The assessment of the experiment is completed by qualitatively comparing the time-averaged flow field with previous studies [see (Moreau *et al.*, 2016)] on the same airfoil and by quantitatively comparing the time-average and turbulent boundary layer profiles obtained from planar and tomographic PIV measurements.

Figure 5 shows the mean flow velocity components V_x and V_y around the CD airfoil in the laboratory reference frame. This was obtained by the superimposition of three planar-PIV measurements performed on the suction-side (M3), on the pressure-side (M2), and in the near-wake (M4), respectively. Contours reveal numerous salient features of the flow around the airfoil. At the leading edge, the flow experiences a favorable pressure gradient; starting from approximately mid-chord, the flow decelerates until the trailing edge; finally, it separates just after the blunt trailing edge. The flow field near the leading edge shows a region near the wall with a

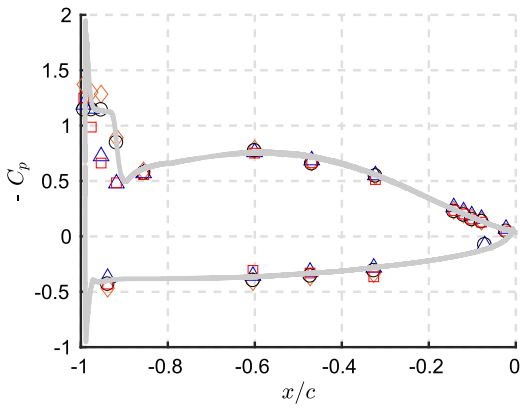

FIG. 4. Mean pressure coefficient C_p for the CD airfoil in different wind tunnel facilities. Legends: orange diamonds—V-Tunnel at TU Delft, black circles—anechoic wind tunnel facility at UdeS, blue triangles—anechoic wind tunnel facility at ECL [see Moreau and Roger (2005), for instance], red squares—wind tunnel facility at MSU [see Neal (2010), for instance], and gray curve—LBM DNS [see Sanjosé *et al.* (2011), for instance].

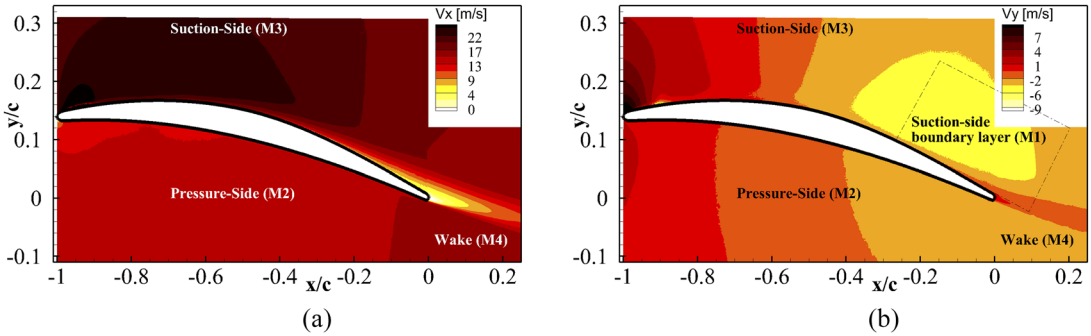

FIG. 5. Mean velocity contours around the airfoil in the laboratory reference frame: (a) streamwise velocity V_x and (b) transverse velocity V_y.

localized higher negative wall-normal velocity component; this corresponds to the location where the plateau in C_p was observed in Sec. III A. For this reason, this can be associated with the presence of a laminar recirculation bubble, which was also observed experimentally and numerically in previous studies [see Moreau and Roger (2005), Neal (2010), Sanjosé *et al.* (2011), Wang *et al.* (2009), and Wu *et al.* (2018), for instance]. Using a stethoscope probe, the flow was verified to transition to turbulence downstream of this location. Because of the relative low resolution of this experimental setup, which was built to capture the time-averaged spatial development of the flow around the CD airfoil, it is not possible to further quantify the effects of the recirculation bubble. However, this goes beyond the scope of the current paper.

The comparison of the time-average (U_i) and rms (u_i') boundary layer profiles at RMP 26 obtained from planar and tomographic PIV measurements is shown in Fig. 6. Very good agreement between the two measurements of the mean boundary layer profile is found, consistent with the previous comparison of planar-PIV data with the DNS data by Wu *et al.* (2018). Some discrepancies for the turbulent fluctuations are caused by the lower spatial resolution of the tomographic PIV experiment below 0.2 δ_{95}, where δ_{95} is the boundary layer thickness. The latter is defined by taking 95% of the local external velocity obtained by checking where the velocity magnitude normal to the wall at RMP 26 becomes constant (as shown in Fig. 5). Furthermore, the limited spatial resolution results in the 3D modulation of the measured flow structure [see Ragni *et al.* (2019), for instance], which further limits the fidelity of the measurements. Close to the wall, high spatial resolution is needed to capture small scale turbulence [see Ahmadi *et al.* (2019), for instance], which explains why discrepancies close to the wall are slightly higher than elsewhere. Nevertheless, the relative intensity of the turbulent fluctuations is well captured.

From the time-averaged boundary layer profile at RMP 26, it is possible to estimate the boundary-layer integral parameters (namely, the displacement thickness δ^*, the momentum thickness Θ, and the shape factor H) and the wall shear stress, τ_{wall}, all relevant for retrieving the surface pressure fluctuations [see Christophe *et al.* (2015), for instance]. The boundary-layer integral parameters, the external velocity U_e, the local streamwise pressure gradient $\frac{dP}{dx_1}$, Clauser's local parameter β_c ($\frac{\theta}{\tau_w}\frac{dP}{dx}$), Coles's integral parameter Π_c, the Reynolds number based on the momentum thickness Re_θ, and the wall shear stress are reported in Table IV for four locations in the trailing-edge region. The wall shear stress is obtained using the plot method of Clauser (1956). Given the fact that the Reynolds number of the present experiment is transitional and the flow encounters a severe adverse pressure gradient near the trailing edge, the fit is performed only in the region $U^+ = {x_2}^+$. As a matter of fact, Monty *et al.* (2011) showed that the classical log-layer region is limited or almost non-existent in these flow conditions. This was verified for

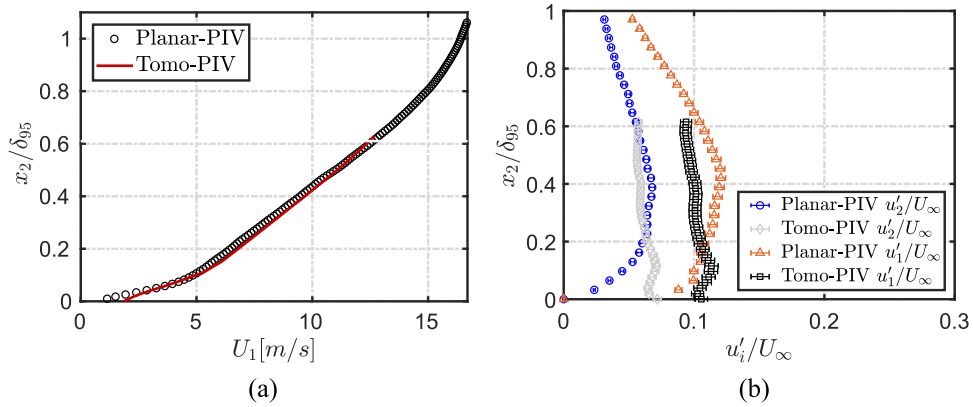

FIG. 6. Comparison of velocity profiles between the two different PIV experiments at RMP 26: (a) mean wall-tangential velocity U_1 and (b) rms velocity components u_i' normalized by the inlet velocity U_∞.

TABLE IV. Boundary layer parameters.

Probe	$\frac{x}{c}$	U_e (m/s)	δ_{95} (mm)	$\delta*$ (mm)	Θ (mm)	H	Re_θ	τ_{wall} (Pa)	Π_c	$\frac{dP}{dx_1}$ (Pa/m)	β_c	δ^+
RMP 26	0.98	17.44	6.34	2.42	1.19	2.03	1350	0.34	2.76	1728	6.08	220
RMP 24	0.9216	17.87	5.34	1.85	0.98	1.89	1135	...	...	...	...	...
RMP 22	0.8806	18.41	4.80	1.56	0.88	1.76	1050	...	...	...	...	...
RMP 21	0.8582	18.77	4.41	1.36	0.82	1.65	997	...	...	...	...	...

the present configuration in Wu's DNS [see Fig. 9 (b) in Wu *et al.* (2019)]. This is also consistent with the Kármán number, δ^+ ($\frac{\delta u_\tau}{\nu}$ with u_τ being the friction velocity), at RMP26, which is about 220. The friction velocity is not reported upstream of RMP 26 because the size of the boundary layer based on the edge velocity decreases rapidly, and the inner scales are so small that a confident estimate of the friction velocity could not be determined using Clauser's method described above. Nevertheless, spatially well resolved velocity data near the trailing edge offer an attractive possibility to determine wall-pressure wavenumber spectra by quantifying the sources responsible for the generation of pressure fluctuations on the surface, as will be shown in Secs. V–VII. Moreover, the results in Table IV show that measurements at RMP 26 agree well with the RANS results reported by Christophe *et al.* (2015) and the recent DNS study of Grasso *et al.* (2019). In fact, the values of δ and τ_{wall} are almost identical at RMP 26.

IV. UNIFIED APPROACH TO STATISTICAL WALL-PRESSURE MODELING

To determine the wall-pressure fluctuations due to a turbulent velocity field convecting over a solid surface, the approach proposed by Kraichnan (1956) is pursued and the source term in Poisson's equation for pressure fluctuations is split into the MS and TT components as

$$\frac{1}{\rho}\nabla^2 p' = \underbrace{-2\frac{\partial u_j}{\partial x_i}\frac{\partial U_i}{\partial x_j}}_{\text{Mean shear}} \underbrace{-\frac{\partial^2}{\partial x_i \partial x_j}(u_i u_j - \overline{u_i u_j})}_{\text{Turbulence-Turbulence}}, \tag{5}$$

where ρ is the density and the overbar stands for a time average. This Poisson's equation stems from the divergence of the incompressible momentum equation, introducing the Reynolds decomposition into mean and fluctuating quantities and then subtracting the time-averaged equation. Equation (5) is subject to two boundary conditions, one outside the shear layer and another at the airfoil surface. The first is based on the fact that p' attains a finite value outside the shear layer; the second is based on the approximation that the derivative of p' in the wall-normal direction goes to zero at the wall [see Kraichnan (1956), for instance]. They can be expressed mathematically as

$$\lim_{x_2 \to \infty} p' = p_0, \tag{6}$$

$$\lim_{x_2 \to 0} \frac{\partial p'}{\partial x_2} = 0. \tag{7}$$

Since the contribution due to the cross term between MS term and TT term is negligible [see Chase (1980), for instance], only the contribution of each source term is considered. Due to limited temporal information, the wavenumber domain was chosen to describe all the source contributions. Further details to yield the latter can be found in Grasso *et al.* (2019).

A. MS source term in wavenumber space

The solution of the MS term in the wavenumber domain is available from the earlier works of Hodgson (1962) and Panton and Linebarger (1974). The latter describes the MS term as a quintuple integral [Eq. (3.5) of Panton and Linebarger (1974)], which, in the local Cartesian co-ordinate reference frame, reads

$$\Pi_{MS}(k_1) = \frac{8{k_1}^2\rho^2}{\pi^2}\iiiii_0^\infty \Big[\frac{1}{k^2}\,e^{-k(x_2'+x_2)}\,R_{22}\,\cos(k_1 r_1) \times \cos(k_3 r_3)\frac{\partial U_1}{\partial x_2}\frac{\partial U_1}{\partial x_2'}u_2'(x_2')u_2'(x_2)\Big] \times dx_2 dx_2' dr_1 dr_3 dk_3. \tag{8}$$

Here, R_{22} is the two-point zero time-lag wall-normal velocity correlation. k_1 and k_3 are the wavenumbers in the wall-tangential and the transverse direction, respectively, while $k = \sqrt{k_1^2 + k_3^2}$ is the wall-parallel wavenumber vector magnitude. r_i is the separation distance in the i-direction. The wall-pressure spectra in the wavenumber space $\Pi_{MS}(k_1)$ is seen to depend on a second-order wall-normal velocity correlation and an interaction term between the mean shear ($\frac{\partial U_1}{\partial x_2}$) and the wall-normal velocity fluctuations [$u_2'(x_2)$].

B. TT source term in wavenumber space

Similar to the MS term, the TT term is expressed in the wavenumber domain. It is worth mentioning that attempts have been made in the past by Hodgson (1962) and more recently by Grasso *et al.* (2019). However, Hodgson (1962) made several assumptions, such as the normal distribution assumption that will be verified here. The present study therefore proposes a new model reported in Eq. (9), which does not invoke the normal distribution assumption, the mathematical description of which is given in the Appendix. The TT term, in the local Cartesian co-ordinate system, reads

$$\Pi_{TT}(k_1) = \frac{2\rho^2}{\pi^2}\iiiii_0^\infty \Big[k^2\,e^{-k(x_2'+x_2)}\,C_{ij,lm}(x_2, x_2', r_1, r_3) \times [\tilde{u_i u_j} - \overline{\tilde{u_i u_j}}](x_2)[\tilde{u_i u_j} - \overline{\tilde{u_i u_j}}](x_2')\,e^{-i(k_1 r_1 + k_3 r_3)}\Big] \times dx_2 dx_2' dr_1 dr_3 dk_3. \tag{9}$$

This source term consists of the fourth-order two-point zero time-delay correlation term $C_{ij,lm}(x_2, x_2', r_1, r_3)$, which can be expressed as

$$C_{ij,lm}(x_2, x_2', r_1, r_3) = \frac{\overline{(u_i u_j - \overline{u_i u_j})(\mathbf{x})(u_l u_m - \overline{u_l u_m})(\mathbf{x}+\mathbf{r}_{1,3})}}{\sqrt{\overline{(u_i u_j - \overline{u_i u_j})^2(\mathbf{x})} \times \overline{(u_l u_m - \overline{u_l u_m})^2(\mathbf{x}+\mathbf{r}_{1,3})}}}. \quad (10)$$

Here, $\mathbf{r}_{1,3}$ is the separation vector in a plane parallel to the wall. $C_{ij,lm}$ is similar to what has been used in the past by several authors to determine jet noise sources [see Morris and Zaman (2010), for instance].

V. CHARACTERIZATION OF MS SOURCE TERMS

The MS source term, given in Eq. (8), consists of the mean shear term due to the variation of the wall-parallel mean velocity in the boundary layer ($\frac{\partial U_1}{\partial x_2}$), the turbulence fluctuations of the wall-normal velocity component [$u_2'(x_2)$], and the two-point correlation of the wall-normal velocity component (R_{22}). The latter is the most intricate to quantify and model. Consequently, to estimate the contribution of the MS term toward the total surface pressure fluctuations, an accurate calculation of the two-point correlation is mandatory. In the present work, the second order two-point zero-delay correlation is denoted by

$$R_{ij}(x_1, x_1', x_2, x_2', x_3, x_3') = \frac{\overline{u_i'(x_1, x_2, x_3) u_j'(x_1', x_2', x_3')}}{\overline{u_i'(x_1, x_2, x_3)} \times \overline{u_j'(x_1', x_2', x_3')}}, \quad (11)$$

where $u_i'(x_1, x_2, x_3)$ is the ith component of the velocity fluctuation at the fixed or reference probe location, while $u_j'(x_1', x_2', x_3')$ denotes the jth component of the velocity fluctuations at the moving probe location. The terms $\overline{u_i'(x_1, x_2, x_3)}$ and $\overline{u_j'(x_1', x_2', x_3')}$ are the standard deviation of the turbulent velocity at the fixed and moving probe location, respectively. Equation (11) is written assuming that the flow is non-homogeneous in all three spatial directions.

The uncertainty in the estimation of R_{22}, $\epsilon_{R_{ij}}$, is defined following Benedict and Gould (1996) as

$$\epsilon_{R_{ij}} = \frac{2}{\sqrt{N}} \times (1 - R_{ij}^2), \quad (12)$$

where N is the number of independent samples and R_{ij} is the value of the correlation coefficient. The number of samples N depends on the integral time scale of the largest structures, τ, and on the total length of recording T. N can then be determined using the Nyquist criterion as

$$N = T/2\tau. \quad (13)$$

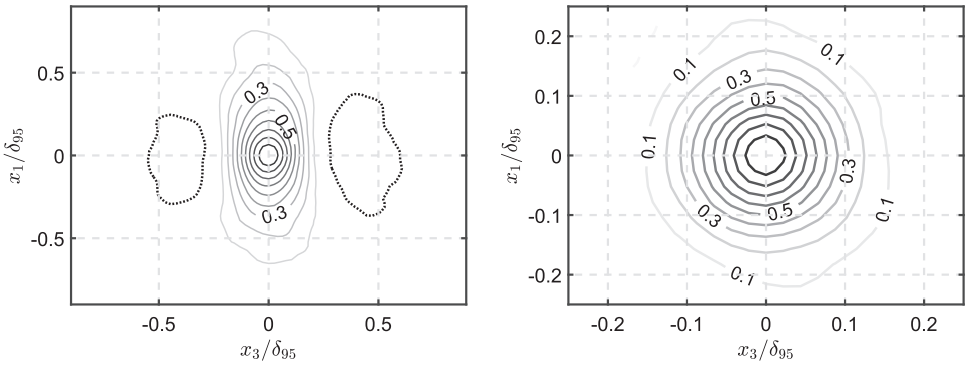

FIG. 7. Tomo-PIV second-order two-point zero time-delay correlation $R_{ij}(x_1, x_1', 0.45 \times \delta_{95}, 0.45 \times \delta_{95}, x_3, x_3')$ in a plane parallel to the wall (iso x_2-cut) at RMP 26 (x_1/C = 0.98): (a) R_{11} and (b) R_{22}. Color transition from the black curve to gray curve indicates decreasing values of correlation, and dotted curves indicate negative values.

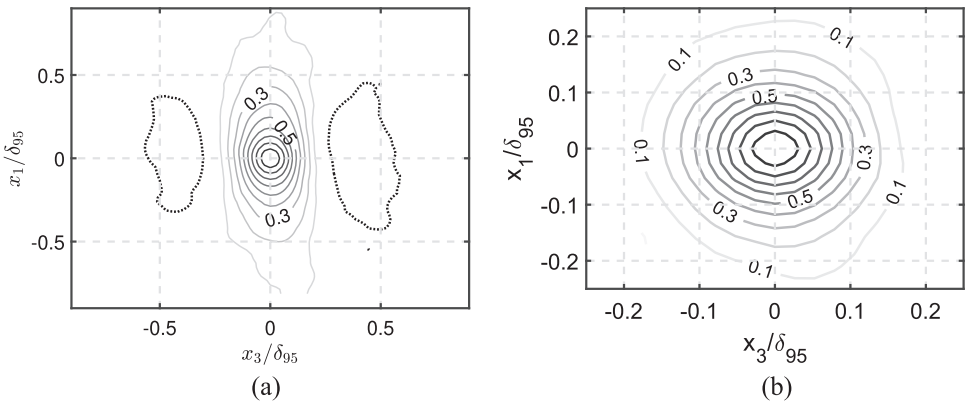

FIG. 8. Tomo-PIV second-order two-point zero time-delay correlation $R_{ij}(x_1, x_1', 0.35 \times \delta_{95}, 0.35 \times \delta_{95}, x_3, x_3')$ in a plane parallel to the wall (iso x_2-cut) at RMP 26 (x_1/C = 0.98): (a) R_{11} and (b) R_{22}. Color transition from black curve to light gray curve indicates decreasing values of correlation, and dotted curves indicate negative values.

For the sake of simplicity, this time scale τ has been estimated based on the largest length scale present in the flow. The latter corresponds to that of the wall-tangential velocity correlation, which is here approximately equal to 1.5–2 times the boundary layer thickness. The convection velocity is chosen to be equal to 0.72 U_∞ based on the recent study by Grasso *et al.* (2019), consistently with all available experimental data.

A. Overall topology of the two-point velocity correlation

Two-point correlations of the streamwise (R_{11}) and wall-normal velocity (R_{22}) in two planes parallel to the wall are shown in Figs. 7 and 8. The R_{11} contours are consistent with the results of the DNS of a turbulent boundary layer subjected to a strong adverse pressure gradient at a slightly larger Reynolds number $\mathrm{Re}_\theta = 1755$ but for a similar shape factor $H = 2$ [Fig. 16 in Gungor *et al.* (2014)]. R_{11} has a main lobe stretched along x_1 surrounded by two negative lobes on each side. This is expected as the correlation flux should vanish in planes perpendicular to the direction of velocity, which, in turn, implies the presence of negative and positive values of correlation (Sillero *et al.*, 2014). Moreover, this is needed to fulfill the continuity equation for an incompressible flow, especially in the direction where the flow is homogeneous [see Townsend (1980), for instance]. The correlation length of the streamwise velocity correlation structures appears to be about 1.5 × δ_{95} in both planes parallel

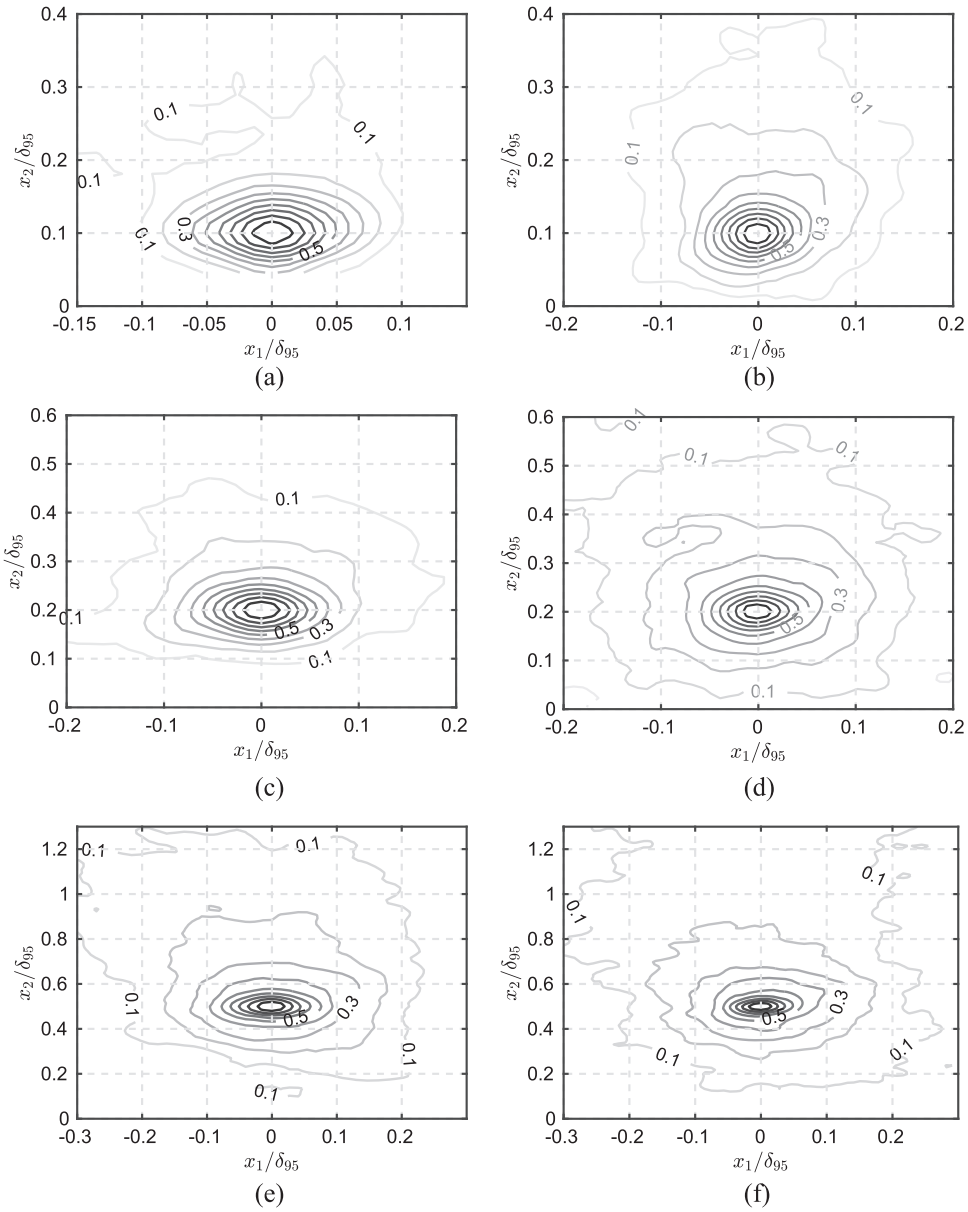

FIG. 9. $R_{22}(x_1, x_1', x_2, x_2', 0, 0)$ in a plane normal to the airfoil (a) at RMP 21 (x_1', 0.1 × δ_{95}, x_2', 0, 0), (b) at RMP 26 (x_1', 0.1 × δ_{95}, x_2', 0, 0), (c) at RMP 21 (x_1', 0.2 × δ_{95}, x_2', 0, 0), (d) at RMP 26 (x_1', 0.2 × δ_{95}, x_2', 0, 0), (e) at RMP 21 (x_1', 0.5 × δ_{95}, x_2', 0, 0), and (f) at RMP 26 (x_1', 0.5 × δ_{95}, x_2', 0, 0). Color transition from black curve to light gray curve indicates decreasing values of correlation.

to the wall located at a distance of 0.35 and 0.45 × δ_{95} from the wall, respectively. The presence of large-scale structures with such a spanwise spacing is consistent with the DNS results of a turbulent boundary layer in the APG zone at a slightly smaller Reynolds number Re_θ = 900 [see Fig. 15(a) in Abe (2019)]. The wall-normal velocity correlation R_{22}, in contrast, seems to be principally stretched in the streamwise direction, consistent with the DNS data of Sillero *et al.* (2014) on a flat plate and that of Grasso *et al.* (2019) on the CD airfoil. Both velocity correlation contours (R_{11} and R_{22}) seem homogeneous in a plane parallel to the wall. Therefore, the anisotropy, i.e., the stretching in the streamwise direction compared to the wall-normal direction, is independent of the separation distance from the fixed point [see Figs. 7 and 8 in Grasso *et al.* (2019)].

B. Self-similarity of the two-point correlation R_{22}

Even if R_{22} is homogeneous in planes parallel to the wall, its anisotropy in planes normal to the wall is clearly shown in Fig. 9. This inhomogeneity is caused by the presence of the wall that affects the normal growth of structures in the wall-normal direction.

To better show the inhomogeneity, the two-point correlation between two points separated by a wall-normal distance $\Delta x_2 = x_2{}' - x_2$ for the same streamwise x_1 and spanwise x_3 location is considered. To simplify the notations, the latter two coordinates are now dropped in Eq. (11) to yield for the wall-normal velocity component,

$$R_{22}(x_2, x_2{}') = \frac{\overline{u_2'(x_2)u_2'(x_2')}}{\overline{u_2'(x_2)} \times \overline{u_2'(x_2')}}. \tag{14}$$

However, as suggested by Hunt *et al.* (1987) and shown analytically by Oberlack (2001), if the correlation is instead divided by the top point and plotted against $x_2{}'/x_2$ (with $x_2 > x_2{}'$), self-similarity is achieved. Therefore, Eq. (14) is multiplied by $\overline{u_2'(x_2')}$ for the moving point $x_2{}'$ and divided by $\overline{u_2'(x_2)}$ for the upper and fixed point x_2 to yield

$$\tilde{R}_{22}(x_2, x_2{}') = \frac{\overline{u_2'(x_2)u_2'(x_2')}}{\overline{u_2'(x_2)} \times \overline{u_2'(x_2)}} = \frac{\overline{u_2'(x_2)u_2'(x_2')}}{\overline{u_2'(x_2)}^2}. \tag{15}$$

The two equations (14) and (15) would yield the same result if the turbulence is homogeneous. However, in the present case of inhomogeneous turbulence, the results will differ [see Kamruzzaman *et al.* (2011), for instance]. Figure 10 shows the results of the two-point correlations near the trailing edge using both normalizations in the wall-normal direction with zero separation in the wall-tangential and transverse directions. Each curve corresponds to a location in the boundary layer, from black close to the wall to light gray in the external layer. In each plot, the black arrows stress that both R_{22} [Fig. 10(a)] and $\tilde{R}_{22}$ [Figs. 10(b)–10(d)] have the same trends when getting close or moving away from the fixed probe for all RMP locations. Moreover, $\tilde{R}_{22}$ plots [Figs. 10(b)–10(d)] show a self-similar behavior for $x_2{}'/x_2 < 0.5$ and all darkest lines that correspond to the near-wall region, at all probe locations, as predicted by Hunt *et al.* (1987) and previous measurements on flat plates. Moving toward the trailing edge, i.e., with increasing mean pressure

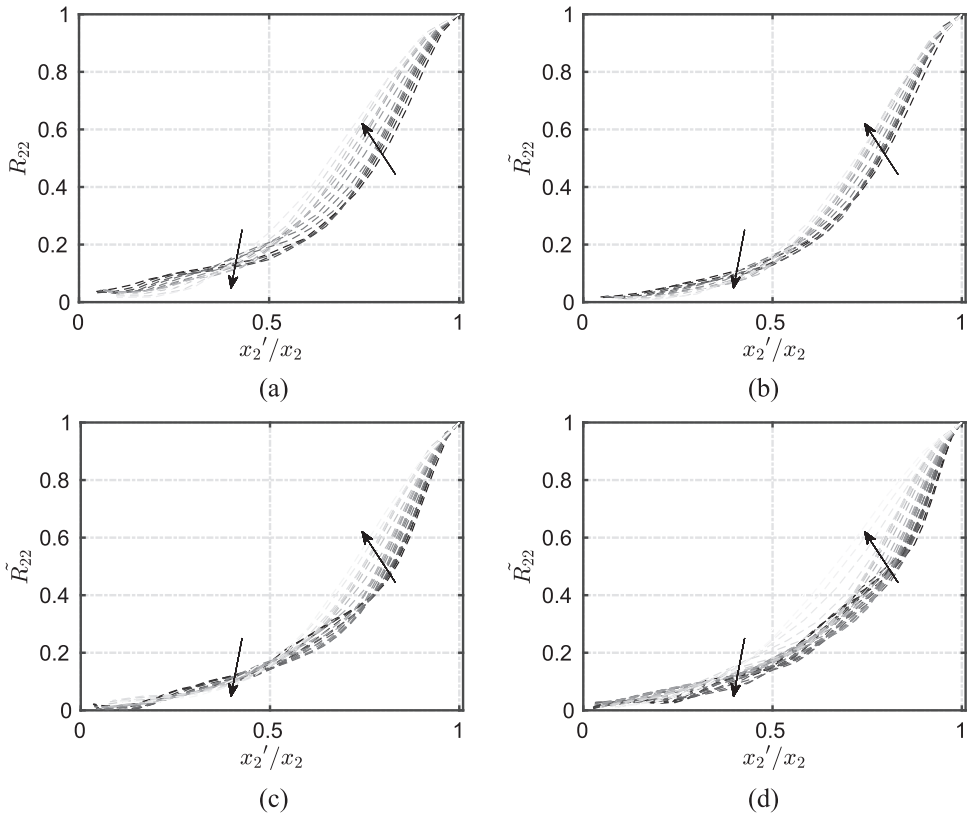

FIG. 10. (a) R_{22} at RMP 21, (b) $\tilde{R}_{22}$ at RMP 21, (c) $\tilde{R}_{22}$ at RMP 24, and (d) $\tilde{R}_{22}$ at RMP 26. The color transition from the black dashed curve to light gray dashed curve indicates the fixed probe location close to the wall and away from the wall, respectively (arrows indicate increasing distance from the wall). The closet probe is taken at one interrogation window away from the wall, while the farthest probe is located at boundary layer displacement thickness δ^*.

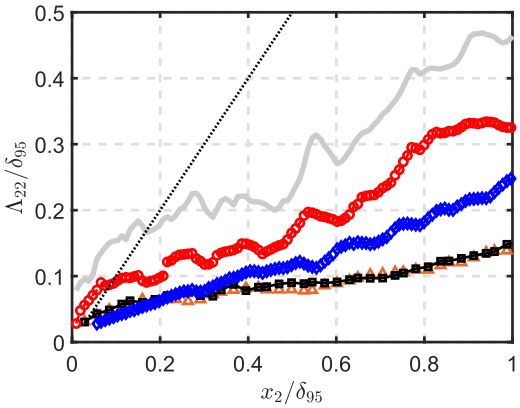

FIG. 11. Wall-normal velocity integral length scale $\Lambda_{22}^{k\pm}$ at RMP 26. Legends: gray curve—$\Lambda_{nl\,22}^{2+}$, red curve with circles—Λ_{22}^{2+}, blue curve with diamonds—Λ_{22}^{2-}, curve with orange triangles—Λ_{22}^{1+}, and black curve with squares—Λ_{22}^{1-}.

gradient from RMP 21 to RMP 26, the self-similarity becomes less pronounced, which is consistent with what Zawadzki *et al.* (1996) observed for non-equilibrium boundary layers.

Figures 9 and 10 discussed above suggest that the effect of blocking becomes weaker as the pressure gradient increases. Furthermore, with increasing pressure gradient, the correlation contours are more tilted, especially near the wall [see Fig. 9(d)]. In summary, close to the wall, blocking has the most dominant effect on the wall-normal velocity correlation profiles. Away from the wall, i.e., toward the regions with a lower blocking effect, the pressure gradient reduces the extent of the two-point correlation of the wall-normal velocity [Fig. 9(e) compared with Fig. 9(f)]. The stronger the adverse pressure gradient, the larger the zone and the less correlated the wall-normal velocity.

C. Wall-normal velocity correlation length

From the two-point correlation, the integral length scales Λ_{ij}^{k} can be computed. This section focuses on the correlation length of the wall-normal velocity component in the wall-normal direction, Λ_{22}^{k}, defined as

$$\Lambda_{22}^{k}(x_2) = \int_0^{\infty} R_{22}(x_2, x_k')\, \mathrm{d}x_k'. \tag{16}$$

Given the asymmetry of the elliptical iso-contours of R_{22} observed in Fig. 9, the integration in Eq. (16) can be split with respect to the center of these ellipses (x_1^c, x_2^c) and four different length scales $\Lambda_{22}^{k\pm}$ can be defined. For instance, in the wall-normal direction, the following length scales $\Lambda_{22}^{2\pm}$ can be defined:

$$\Lambda_{22}^{2-}(x_2) = \int_{x_2^c}^{0} R_{22}(x_2, x_2')\, \mathrm{d}x_2'$$

and

$$\Lambda_{22}^{2+}(x_2) = \int_{x_2^c}^{\infty} R_{22}(x_2, x_2')\, \mathrm{d}x_2', \tag{17}$$

where the + sign underscores the direction in which x_2 increases, while the − sign underscores the direction in which x_2 decreases. A similar convention has been applied in the streamwise direction.

In the following, the infinite integration limits are set as the points in the wall-normal direction where the co-variance is lower than 5% of the maximum value. The length scale computed with this approach is compared to the length scale obtained without any volume truncation ($\Lambda_{nl\,22}^{2+}$) in Fig. 11. The comparison confirms that not including the integration limits results in a larger value of the integral length scale. The figure further confirms the flow non-homogeneity discussed above. The following inequality, $\Lambda_{22}^{1}(x_2) \le \Lambda_{22}^{2-}(x_2) \le x_2$, is also verified, which suggests the absence of any eddy larger than the height x_2. This, in turn, explains the low-frequency plateau seen below in S_{22}.

Figure 12 shows the integral length scales $\Lambda_{22}^{2\pm}$ in the airfoil aft, APG zone on the suction side. As expected, both correlation lengths increase when moving away from the wall (larger turbulent scales), and they decrease downstream with increasing mean APG. This is enhanced away from the wall, as shown in Fig. 12(a). Furthermore, blocking makes the integral correlation Λ_{22}^{2-} curves almost self-similar when the fixed/reference probe is taken near the wall irrespective of the pressure gradient [see Fig. 12(b) for $x_2'/x_2 \le 0.5$ and the black lines], confirming that blocking supersedes the effect of APG close to the wall. This is consistent with the self-similar

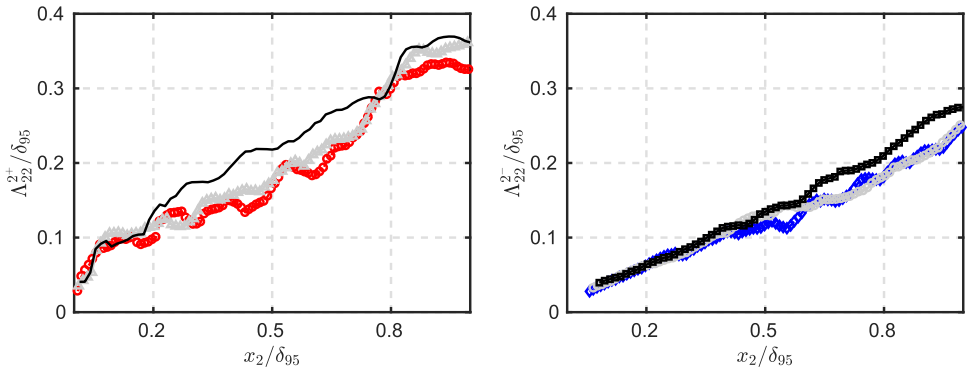

FIG. 12. Effect of an Adverse Pressure Gradient (APG) on $\Lambda_{22}^{2\pm}$. (a) Λ_{22}^{2+}: red curve with circles—RMP 26, gray curve with triangles—RMP 24, and black curve—RMP 21; (b) Λ_{22}^{2-}: blue curve with diamonds—RMP 26, gray curve with circles—RMP 24, and black curve with squares—RMP 21.

curves in Fig. 10 near the wall, even though while calculating the integral correlation length we have normalized co-variance values with the standard deviation of velocity at moving and fixed points. Finally, it should be noted that Λ_{22}^{2+} is always larger than Λ_{22}^{2-} and that the self-similarity is preserved longer for Λ_{22}^{2-} because of the wall blocking.

VI. MODELING OF THE MS SOURCE TERM

Sections V A–V C have assessed the competing effects of the streamwise mean pressure gradient and the crosswise variation of the mean shear induced by the airfoil surface. Furthermore, the effect of wall blocking on the two-point velocity correlation in the presence of a mean pressure gradient has been quantified. The next step is to test the existing models and propose some extensions.

A. Modeling of the wall-normal velocity correlation

The two-point correlation has been modeled in the past assuming isotropic turbulence [see Batchelor (1953), for instance]. For the case of flow past an airfoil, as shown in Sec. V, turbulence is generally anisotropic and inhomogeneous. Nevertheless, in a plane parallel to the wall, it was shown that both wall-tangential and normal velocity fluctuations are almost homogeneous. Figure 13 shows a graphical representation of the wall-normal velocity fluctuations in a plane perpendicular to the wall. Thus, it can be expected that a model assuming isotropic turbulence for the wall-normal velocity performs poorly. These can be improved either by taking into account inhomogenous effects, e.g., blocking of eddies by the wall [see Hunt and Graham (1978), for instance], or by modifying the isotropic turbulence models based on the experimental results presented in Sec. V. However, Hunt and Graham (1978) theory can neither be analytically integrated to give a closed-form expression for the two-point velocity correlation nor does it account for flow anisotropy in a plane parallel to the wall. Therefore, in the remainder of this section, we explore improvements of the isotropic turbulence models based on the observations made in Sec. V to account flow anisotropy and inhomogeneity.

The wall-normal velocity two-point correlation for isotropic turbulence is given by

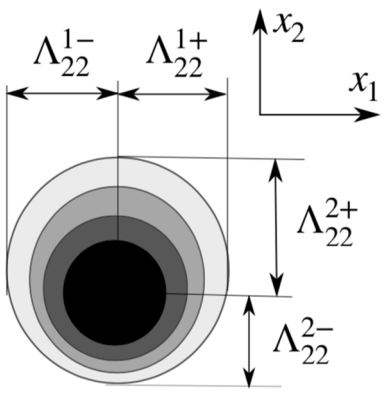

FIG. 13. Eddy structure of the wall-normal velocity in a plane normal to the airfoil.

$$R_{22}(r_1, r_2, r_3) = F(\mathbf{r}) + \frac{{r_1}^2 + {r_3}^2}{2\mathbf{r}} \frac{dF}{d\mathbf{r}}, \tag{18}$$

where r is the norm of the separation vector [see Batchelor (1953), for instance]. Following Wilson (1997) or Grasso *et al.* (2019), the longitudinal correlation function for homogeneous and isotropic turbulence, $F(\mathbf{r})$, can be given by the generalized von Kármán model,

$$F(\mathbf{r}) = \frac{1}{2^{\nu-1}\Gamma(\nu)} \left(\frac{\mathbf{r}}{l_y}\right)^{\nu} K_{\nu}\left(\frac{\mathbf{r}}{l_y}\right), \tag{19}$$

where $\nu = 1/3$ yields the classical von Kármán model [see von Kármán (1948), for instance], $\nu = 1/2$ yields the Liepmann's model [see Liepmann *et al.* (1951), for instance], and $\nu = 7/6$ yields the Rapid Distortion Theory (RDT) model proposed by Hunt (1973).

Similarly, the transverse correlation function $G(\mathbf{r})$ for homogeneous and isotropic turbulence is given by

$$G(\mathbf{r}) = \frac{1}{2^{\nu-1}\Gamma(\nu)} \left(\frac{\mathbf{r}}{l_y}\right)^{\nu} \times \left[(\nu+1) K_{\nu}\left(\frac{\mathbf{r}}{l_y}\right) - \frac{1}{2}\left(\frac{\mathbf{r}}{l_y}\right) K_{\nu+1}\left(\frac{\mathbf{r}}{l_y}\right)\right], \tag{20}$$

where K_ν is the modified Bessel function of the second kind of order ν. The generalized correlation length l_y is proportional to Λ as

$$l_y = \frac{\Gamma(\nu)\Lambda}{\sqrt{\pi}\Gamma(\nu + 0.5)}, \tag{21}$$

where, for isotropic turbulence, Λ is obtained from a single point measurement [see Hinze (1975) and Wilson (1997), for instance]. However, based on the observations made in Sec. V, two length scales Λ_{22}^{2+} and Λ_{22}^{2-} need to be defined to account for flow inhomogeneity in the wall-normal direction, in addition to the transverse length scales Λ_{22}^{1} and Λ_{22}^{3} to account for flow anisotropy in wall-parallel planes. Since inhomogeneity due to wall blocking is an important phenomenon, which cannot be accounted for by using transverse length scales, it narrows our choice to longitudinal length scales Λ_{22}^{2+} and Λ_{22}^{2-}. Among them, however, Λ_{22}^{2-} does not reflect any effect of the mean-pressure gradient, especially close to the wall [see Fig. 12(b)].

The integral of the correlation functions $F(\mathbf{r})$ and $G(\mathbf{r})$ results in the integral correlation length scales Λ and $\Lambda/2$, respectively. As a result, in the isotropic correlation model, the transverse length scale is always half the longitudinal length scale. Figure 11 shows that the longitudinal length scale Λ_{22}^{2+} is approximately half the transverse length scale Λ_{22}^{1}. Therefore, the decay of R_{22} in the transverse direction can be correctly modeled using the longitudinal length scale Λ_{22}^{2+} as input for the isotropic correlation model. Thus, the present paper will use Λ_{22}^{2+} as the appropriate length scale to take into account the effect of mean-shear, blocking, and mean adverse pressure gradient.

The second parameter to be determined for the isotropic model [Eq. (18)] is the order of the modified Bessel function ν that controls the rate of correlation decay. Previous studies found that the exponential decay ($\nu = 0.5$) provides the best estimation [see Kamruzzaman *et al.* (2011) and Panton and Linebarger (1974), for instance],

while Grasso *et al.* (2019) observed further improvements using the rapid distortion theory (ν = 7/6) instead. In the present study, we find that the isotropic turbulence model with ν = 0.5 and Λ_{22}^{2+} as the length scale already gives a fair comparison with the experimental measurements in the wall-tangential direction, as shown in Fig. 14. However, the isotropic model with these parameters (length scale and ν) overestimates the extent of R_{22}, as shown in Fig. 15, due to flow inhomogeneity in the wall-normal (vertical) direction, which leads to a reduction in the correlation length (compared to the points away from the wall). Figure 15 also shows that the exponential decay function with correlation length Λ_{22}^{2+} estimates well the decay of R_{22} over a shorter separation distance, while it underestimates the value of R_{22} for a larger separation. However, when Λ_{nt22}^{2+} is used as the length scale in the exponential decay function, the generalized model estimates R_{22} better for large separation distances, while it is less accurate for small distances. Therefore, it appears that none of the length scales Λ_{nt22}^{2+} or Λ_{22}^{2+} is universally applicable for modeling R_{22}. Changing the exponential decay to a Gaussian one did not result in any further improvement.

B. Characterization of flow inhomogeneity

Panton and Linebarger (1974) proposed to model R_{22} by expressing the correlation length as a function of both the moving

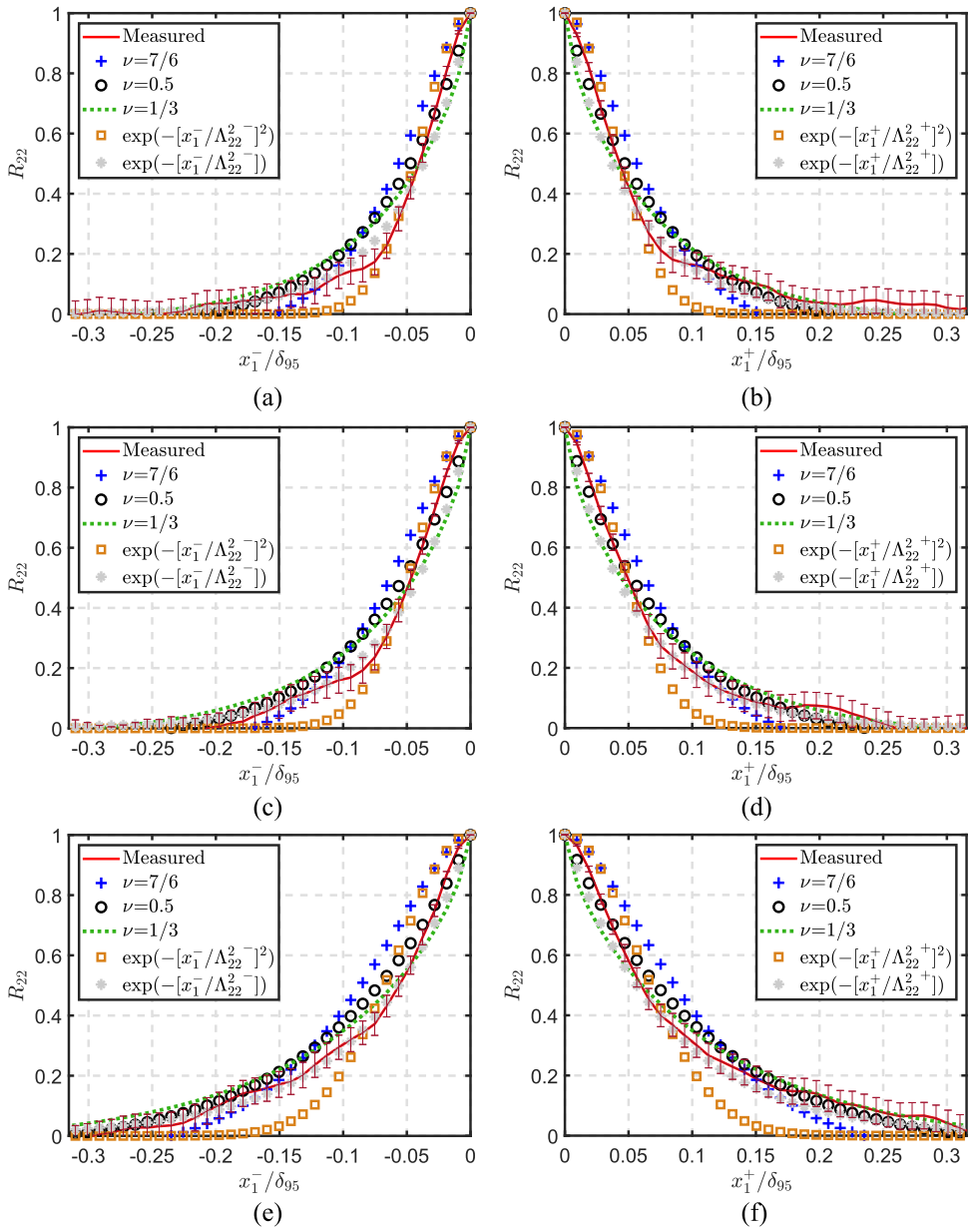

FIG. 14. Two-point wall-normal velocity correlation R_{22} with moving point traversing in the wall-tangential direction, i.e., (x_1). The fixed points for top, middle, and bottom plots are at (x_1 = RMP 26; x_2 = 0.1 × δ_{95}), (x_1 = RMP 26; x_2 = 0.2 × δ_{95}), and (x_1 = RMP 26; x_2 = 0.5 × δ_{95}), respectively. [(a), (c), and (e)] Moving points traveling upstream, i.e., $x_1'^-$, and [(b), (d), and (f)] moving points traveling downstream, i.e., $x_1'^+$.

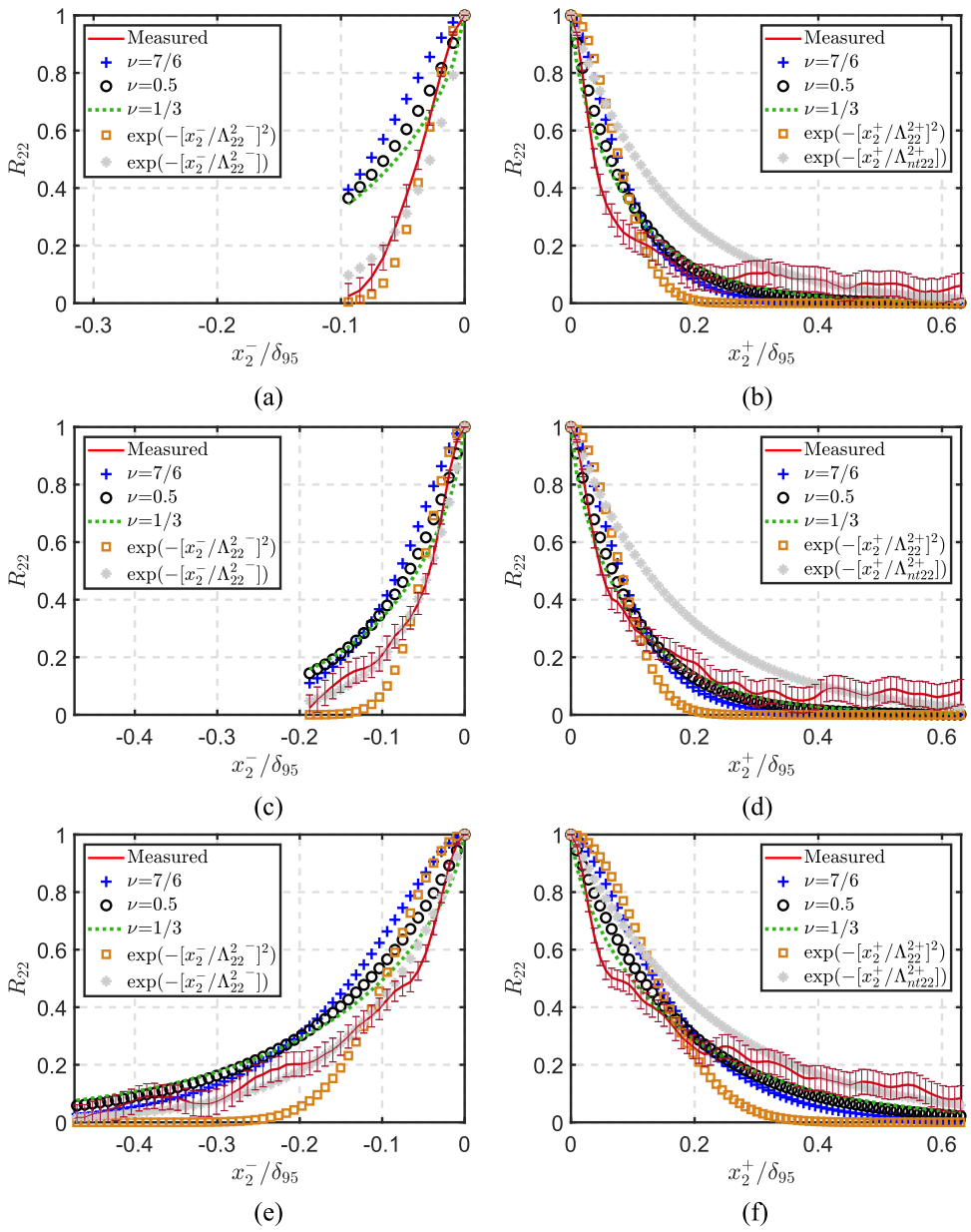

FIG. 15. Two-point wall-normal velocity correlation R_{22} with moving point traversing in the wall-normal direction, i.e., (x_2). The fixed points for top, middle, and bottom plots are at (x_1 = RMP 26; x_2 = 0.1 × δ_{95}), (x_1 = RMP 26; x_2 = 0.2 × δ_{95}), and (x_1 = RMP 26; x_2 = 0.5 × δ_{95}), respectively. [(a), (c), and (e)] Moving points traveling toward the wall, i.e., $x_2'^-$, and [(b), (d), and (f)] moving points traveling away from the wall, i.e., $x_2'^+$.

and fixed point variables, i.e., $\Lambda_{22}^{i^+}[x_2, x_2']$. The length scale used by Panton and Linebarger (1974) was computed by curve fitting $R_{22}(r_1, 0, 0)$, $R_{22}(0, r_2, 0)$, $R_{22}(0, 0, r_3)$ obtained from the hot-wire measurements of Grant (1958). Panton and Linebarger (1974) also used stretching factors to account for the flow anisotropy in the wall-parallel direction. Even though Figs. 7 and 9 suggest that most of the distortion of the correlation contours of R_{22} is found in the wall-normal direction, a single flow anisotropy factor is insufficient to describe the three-dimensional character of R_{22}. Furthermore, as discussed in Sec. VI A, Λ_{22}^{2+} is a more appropriate scale to use to quantify the effect of mean-shear, blocking, and mean adverse pressure gradient. We therefore suggest the following anisotropy scaling factors:

$$\alpha = 2\Lambda_{22}^{1}/\Lambda_{22}^{2^+}, \beta = 2\Lambda_{22}^{3}/\Lambda_{22}^{2^+}, \gamma = \Lambda_{22}^{1}/\Lambda_{22}^{3}. \tag{22}$$

The anisotropy scaling factors in Eq. (22) reduce to 1 under the assumption of isotropic turbulence, where the transverse length scale is twice the longitudinal length scale. Furthermore, the stretching parameters as defined in Eq. (22) are interdependent; for instance, it can be shown that $\alpha = \gamma \times \beta$. Using these definitions of the stretching parameters and the exponential decay function, Eq. (18) for the two-point correlation becomes

$$R_{22}(x_2, x_2', r_1, r_3) = \left[1 - \frac{\mathbf{r}_{13}^2}{\sqrt{\mathbf{r}_{13}^2 + (x_2 - x_2')^2} \times 2\Lambda_{22}^{2+}}\right] \times \exp\left(-\frac{\sqrt{\mathbf{r}_{13}^2 + (x_2 - x_2')^2}}{\Lambda_{22}^{2+}}\right), \quad (23)$$

where $\mathbf{r}_{13}$ is now given by $\mathbf{r}_{13} = \left(\frac{r_1}{\alpha}\right)^2 + \left(\frac{r_3}{\beta}\right)^2$.

$\Lambda_{22}^{2+}[x_2, x_2']$ is expressed as a function of both the moving point (x_2') and the fixed point (x_2) variables by defining it as the geometric mean of the length scales at these two locations. The geometric mean is chosen since it is always smaller than the arithmetic mean for finite separation and may thus better reflect compression of wall-normal velocity correlations due to the solid wall. A detailed comparison is shown in Fig. 16 to verify the advantage of a combined function with respect to the more conservative, yet recent, approaches of Slama *et al.* (2018) and Grasso *et al.* (2019).

Figure 16(a) illustrates that the model of Slama *et al.* (2018) results in elongated and tilted correlation contours. The tilt angle of the correlation contours proposed by Slama *et al.* (2018) is not well-tuned for the present case. Furthermore, the model fails to capture the true extent of R_{22} in the wall-tangential direction. More importantly, the model does not capture the compression of correlation contours near the wall because of the assumption of homogeneity in the wall-normal direction inherent in the model of Slama *et al.* (2018). The experimental results are further compared with the model proposed by Grasso *et al.* (2019) in Fig. 16(b). Grasso *et al.* (2019) used modified isotropic turbulence to model S_{22} (and hence R_{22}) where Λ_{11}^1 was chosen as the reference length scale and defined it as a function of both moving and fixed-point variables by taking the algebraic mean of the length scales between those two points. The orientation of the contours is significantly improved, and a fair comparison with the experiment is obtained away from the wall. However, the model does not compare favorably to the reference data close to the wall. A possible explanation lies in the choice by Grasso *et al.* (2019) of Λ_{11}^1 to model R_{22}. Note that such an assumption was mostly driven by similar reference length scale selection in previous models such as the TNO-Blake modeling approach. As shown in Figs. 7 and 8, the overall shape of the two correlations R_{11} and R_{22} is strikingly different. Furthermore, the effect of blocking is not as pronounced in the streamwise velocity correlations R_{11} as it is in the case of R_{22}. Consequently, by using Λ_{11}^1 to model R_{22}, the model of Grasso *et al.* (2019) does not reflect the compression of R_{22} contours close to the wall [see Fig. 9(b), for instance]. Figure 16(c) clearly shows that the proposed model better estimates the overall extent of R_{22} in both wall-normal and wall-tangential directions and better reproduces the compression of R_{22} close to the wall. Any further improvement requires consideration of anisotropy. We thus follow Panton and Linebarger (1974) to consider the variation of anisotropy as a function of wavenumber and distance from the wall, which requires

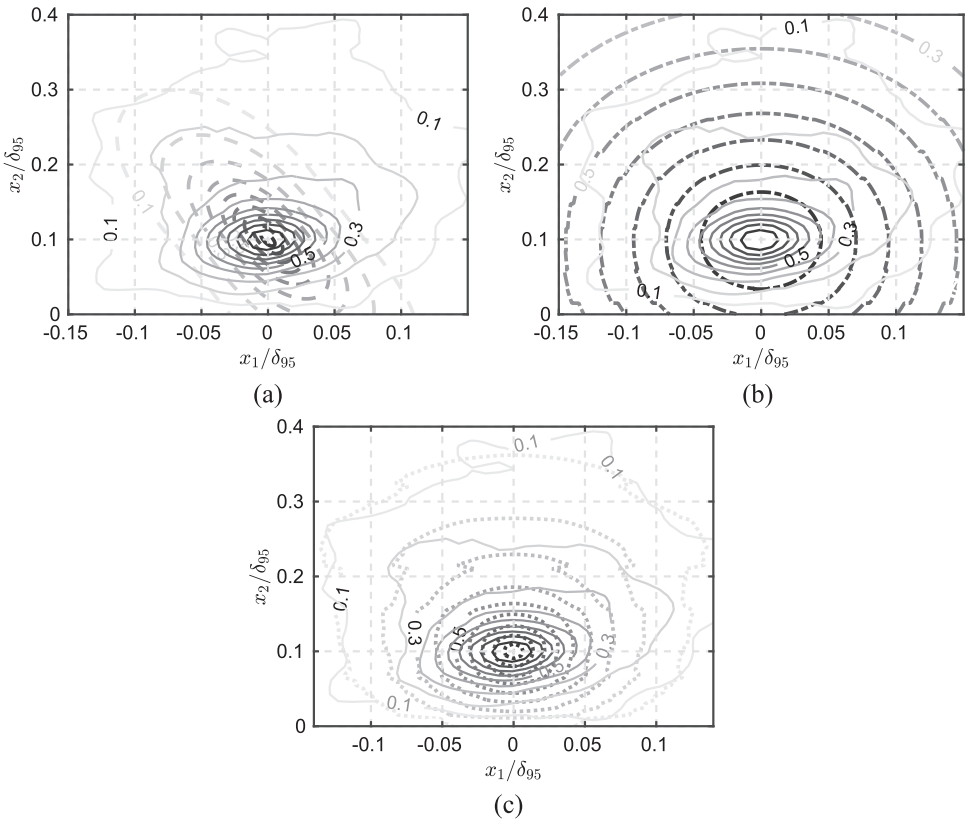

FIG. 16. Effect of wall-normal inhomogeneity on the wall-normal velocity correlation modeling. Black solid curves—PIV data. (a) Black dashed curves—R_{22} model of Slama *et al.* (2018), (b) Black dashed-dotted curves—R_{22} model of Grasso *et al.* (2019), (c) Black dotted curves—modified model of Panton and Linebarger (1974). The color transition from the black curve to light gray curve represents decreasing correlation.

to move from the real domain to the Fourier (wavenumber) domain.

C. Characterization of flow anisotropy

The flow anisotropy is quantified using the wavenumber spectrum of the wall-normal velocity component, $S^1_{22}(k_1) \equiv S_{22}(k_1, 0, 0)$ (Fig. 17). Such wavenumber spectra have been computed using the planar-PIV data because they have a higher dynamic range than the TR-Tomo PIV measurement. The dynamic range of PIV, which is defined as the ratio between the sensor size and the particle image diameter, sets the measurement range of the velocity wavenumber spectra [see Adrian *et al.* (2011), for instance]. While the low wavenumber limit of the wall-normal velocity spectra is determined by the field of view, the high wavenumber cutoff depends on the size of the final window [see Foucaut *et al.* (2004), for instance].

To isolate the effects of the wall, the wavenumber energy spectra are first computed removing the near-wake region from the vector field [Fig. 17(a)] and then computed using the entire vector field [Fig. 17(b)]. Comparing the two figures, it is evident that the presence of the wall causes a plateau in the spectrum near the wall (for low wavenumbers below 2000), in agreement with the findings of De La Riva *et al.* (2004) and Lee and Hunt (1991). The presence of a plateau in the wall-normal velocity spectra bounded by the wall is caused by splatting [see Perot and Moin (1995) and Thomas and Hancock (1977), for instance] wherein the intercomponent energy transfer between the velocity components occurs near the wall.

When the wake region is included in the estimation of the wavenumber energy spectra, peaks appear near the wall at approximately $k_1 = 2.6 \times 10^3$, which closely corresponds to the trailing edge thickness where the flow undergoes separation.

Figure 17(a) further shows that the slope of the wavenumber spectra is shallower closer to the wall, while it becomes $-\frac{5}{3}$ away from the wall. The latter exponent corresponds to the traverse spectra of the wall-normal velocity fluctuations in the wall-tangential direction for isotropic turbulence (same as the longitudinal one). This reveals that the spectra S^1_{22} are also a function of the wall-normal distance, which is not accounted for in the TNO-model [see Stalnov *et al.* (2016), for instance]. Therefore, the use of the isotropic turbulence model (using a constant slope of $-\frac{5}{3}$, for instance) with stretching parameters to integrate the effect of flow anisotropy has a significant limitation. Moreover, the fitting function was originally devised by von Kármán for isotropic turbulence. The aim is thus to capture the variation in the wavenumber by a correctly adapted value of anisotropy.

Due to its success in capturing the correct shape of the correlation function, we use the exponential decay function to model the wavenumber spectra model. The exponential decay model of the two-point correlation transforms into the Liepmann spectra in the Fourier space,

$$S^1_{22}(k_1) = \frac{{u_2}'^2 \Lambda^1_{22}}{\pi} \frac{1 + 3(k_1 \Lambda^1_{22})^2}{[1 + (k_1 \Lambda^1_{22})^2]^2}. \tag{24}$$

Similar to Eq. (20), Eq. (24) can be modified to accommodate the fact that turbulence is not isotropic by making sure that the integral of Eq. (24) is equal to ${u_2}'^2$. However, as the boundary layer grows along the suction side of the airfoil, the mean shear continuously increases ${u_2}'$ along the wall-tangential direction. Hence, to take this growth into account, the value of ${u_2}'^2$ was spatially averaged in the wall-tangential direction for a given wall-normal location, and the correlation length taken for the fitting function is Λ^1_{22}. The results show that the Liepmann spectra can model the wall-normal velocity spectra, especially away from the wall [see Fig. 18(a)] where the effect of both mean shear and blocking is negligible. Close to the wall, while the Liepmann spectra seem to capture the trend of the experimental measurements, it underestimates the spectral contribution of small scales in the $1–2 \times 10^4$ streamwise wavenumber range. This is expected since the Liepmann fitting function is based on a single length scale that corresponds to the most energetic eddy. These results are coherent with its Fourier transform analog (Fig. 14).

To calculate the anisotropy coefficient α [see Eq. (22)] as a function of wavenumber, the path of Panton and Linebarger (1974) and Linebarger (1972) is followed. Although α varies quite significantly at low frequencies for a given wall-normal location, at mid- and high frequencies, the curves collapse, and α can be treated as a function of wavenumber as proposed by Linebarger (1972) and Panton and Linebarger (1974). At low frequencies, on the other hand, α seems to be only a function of the distance to the wall x_2. As can be expected, when these values of anisotropy are accounted for, the modified isotropic turbulence results in even a better estimation (see Fig. 19). Hence, to successfully model the two-point velocity

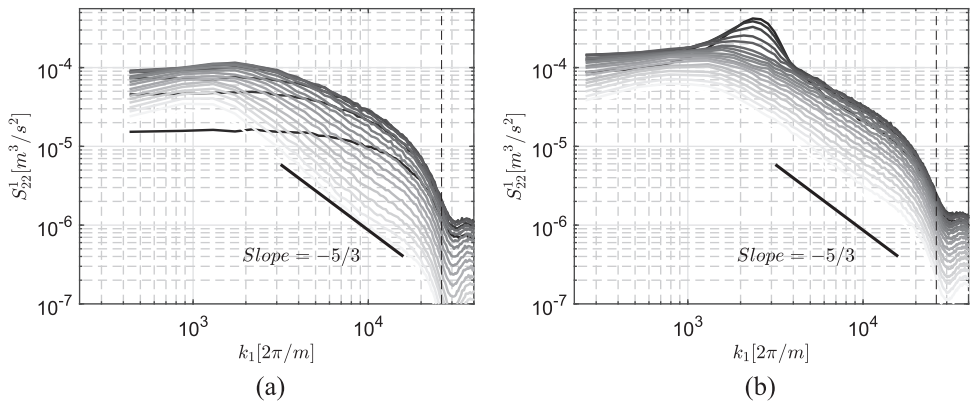

FIG. 17. S^1_{22} wavenumber energy spectra. (a) Measurement domain without the wake. (b) Entire measurement domain. Legends: The color transition from the black curve to light gray curve indicates fixed probe location close (x_2 = 0.037 × δ_{95}) to the wall and away ($x_2 = \delta_{95}$) from the wall, respectively. Black dashed curve—cutoff based on the interrogation window size.

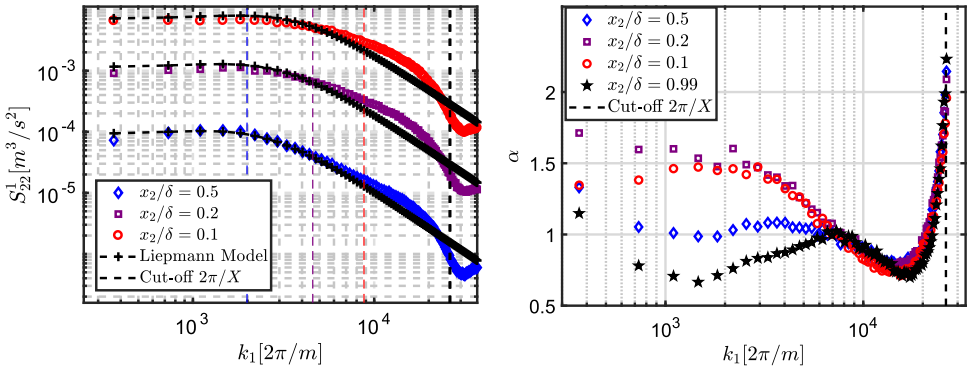

FIG. 18. S_{22}^1 wavenumber energy spectra: (a) Liepmann's model against measurements and (b) anisotropy as a function of wavenumber and distance to the wall.

correlation in the wall-normal direction, the model must be defined as a function of both fixed and moving points along with proper stretching parameters. This conclusion provides an answer to the second objective of this study.

The anisotropy coefficient γ, as shown in the iso-contours of R_{22} in Figs. 7 and 8, appears to be stretched in the wall-tangential direction for most parts of the boundary layer except close to the outer edge of the boundary layer as confirmed by Grasso *et al.* (2019). However, because of flow homogeneity in planes parallel to the wall, an important conclusion can be drawn about the anisotropy coefficient γ: it is unaffected by the mean adverse pressure gradient near the trailing edge. This also explains why Grasso *et al.* (2019) did not notice any variation of γ or of the length $\Lambda_{11}^{1\pm}$ scale in the wall-tangential direction.

D. Modeling of the integral length scale

Modeling of the integral length scale $\Lambda_{ij}^{k\pm}$ hitherto has been limited to semi-empirical approaches. Several authors in the past have attempted to employ Prandtl's mixing length theory to quantify the wall-normal velocity correlation length Λ_{22}^{2+} [see Kamruzzaman *et al.* (2011), for instance]. TNO-Blake models [see Kamruzzaman *et al.* (2011), Parchen (1998), and Stalnov *et al.* (2016), for instance] use mixing length theory in conjunction with empirical scaling. In these models, the length scale Λ_{22}^{2+} is given by the ratio l_m/κ, where l_m is the mixing length and κ is the von Kármán constant. On the other hand, Panton and Linebarger (1974) stated that the correlation length Λ_{22}^{2+} should either be equal to $1.5 \times l_m$ or can be modeled using an empirical model [see Eq. (2.20) of Panton and Linebarger (1974)]. The former relation has been used by Remmler *et al.* (2010) to model Λ_{22}^{2+}, while the latter one was used by Grasso *et al.* (2019). Nevertheless, as shown in Fig. 20, either of them yields similar prediction. However, as shown in Fig. 20, the mixing length theory fails to predict the length scales Λ_{22}^{2+} away from and very close to the wall. This poor comparison between the model and measurements can be due to a couple of reasons. First, it appears from the DNS results of Sillero *et al.* (2014) and PIV data that the length scale Λ_{22} does not approach zero as quickly as the mixing length theory predicts. This is due to the length scales close to the wall not obeying the strong decay of either the mean shear or the wall-normal turbulence velocity. Therefore, close to the wall, length scales based on inner layer variables appear most suited to model the correlation length. Hunt *et al.* (1987, 1989) and later Hunt and Morrison (2000) proposed a length scale model based on shear and wall scales,

$$(\Lambda_{22}^{k+})^{-1}(x_2) = \underbrace{a_b^k \times \frac{1}{x_2}}_{\text{Blocking term}} + \underbrace{a_s^k \times \frac{dU_1/dx_2(x_2)}{u_2'(x_2)}}_{\text{Shear term}}. \tag{25}$$

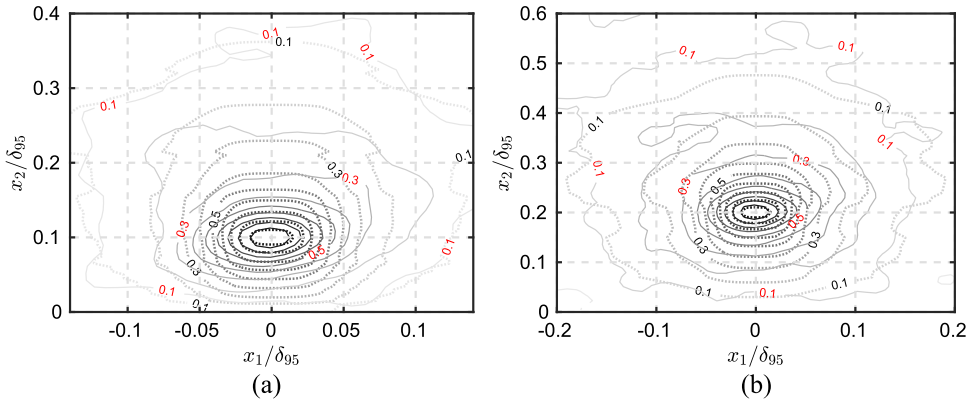

FIG. 19. Two-point correlation R_{22} from the PIV data (black solid curves) and anisotropy tuned model (black dashed curves) (a) at fixed point $0.1 \times y/\delta_{95}$ and (b) at fixed point $0.2 \times y/\delta_{95}$. The color transition from the black curve to light gray curve represents decreasing correlation.

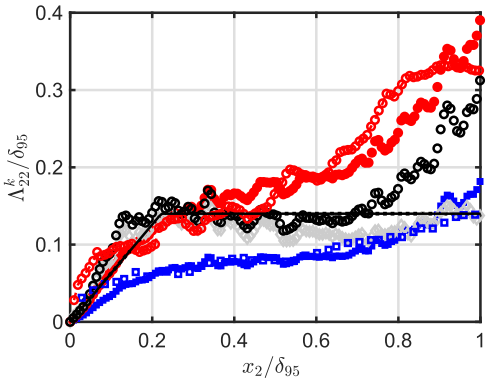

FIG. 20. Modeling of the wall-normal velocity integral length scale $\Lambda_{22}^{k\pm}$. Legends: blue curve with open squares—Λ_{22}^{1+}; blue curve with filled squares—Λ_{22}^{1+} from Eq. (25); red curve with open circles—Λ_{22}^{2+}; red curve with filled circles—Λ_{22}^{2+} from Eq. (25); black open circles—$\frac{u_2'}{dU_1/dx_2 \times \kappa}$; gray open diamonds—Prandtl's mixing length scale [Eq. (7) of Remmler *et al.* (2010)]; and black solid curve— empirical model of Panton and Linebarger (1974).

Equation (25) actually consists of two terms, namely, the blocking term and the shear term. Their relative importance is determined by the empirical constants a_b^k and a_s^k, respectively. In fact, for our case, the length scale based on u_2' and dU_1/dx_2 was found to estimate the mixing length scale if u_2' is allowed to be a function of x_2, as shown in Fig. 20. Note again that the introduction of the von Kármán constant yields a proper length scale from this new mixing length. Hence, the contribution of the shear can be determined by using the length scales obtained from their combination, and these terms also constitute the source terms of the MS term. The blocking term is only a function of x_2, the location of the fixed point. In fact, it enforces the correlation length to linearly decrease while approaching the wall, which can be seen in the correlation contours in Fig. 9. Equation (25) can be first applied in the streamwise direction to yield the constants $a_b^1 = 1.6$ and $a_s^1 = 0.5$ for the wall-normal velocity correlation Λ_{22}^{1+}. These constants have been obtained by a least-square curve-fit of the measured spatial correlation length reported in Fig. 20. They have the very order predicted by Hunt *et al.* (1989) and Hunt and Morrison (2000). The same model can be used to model the wall-normal velocity correlation in the wall-normal direction Λ_{22}^{2+}. The two constants then become $a_b^2 = 1$ and $a_s^2 = 0.2$, respectively. Thus, for the third objective of the paper, the combination of both wall-blocking and shear needs to be taken into account to quantify the wall-normal velocity correlation length correctly. Moreover, the model of Hunt and Morrison (2000) should be preferred over the mixing length theory, which does not reflect the effects of blocking.

VII. TT SOURCE TERM DESCRIPTION AND MODELING

Having characterized the MS terms, the present section seeks to characterize and model TT source terms. As mentioned before, the first attempt to describe the TT source term in the wavenumber domain was undertaken by Hodgson (1962). However, as already pointed out by Grasso *et al.* (2019), Hodgson (1962) had made several key assumptions while deriving the final expression for the wavenumber spectra of the wall-pressure fluctuations due to the TT term. One such key assumption is that the turbulence statistics follows a normal distribution [see Millionshchikov (1941), for instance]. To test this, we calculated the flatness factor or kurtosis using our planar-PIV data at two different streamwise locations. The uncertainty in the kurtosis, $\epsilon_{u_i'^4}$, is given by Benedict and Gould (1996),

$$\epsilon_{u_i'^4} = 1.96 \times \left[\sqrt{\frac{96}{N}}(u_i'^2)^2\right], \tag{26}$$

with N given by Eq. (13). Equation (26) yields the largest uncertainty of 43% ($u_i'^2$) for the present measurements (see Table III). Our measurements reveal that, although the flatness factor of the wall-tangential velocity follows the normal distribution, the values of the flatness factor of the wall-normal velocity are much higher. This is the case especially near the wall, as can be seen from Fig. 21. Note that higher values of the flatness factor especially of the wall-normal velocity have been reported in the past by Kim (1989) and Chang (1998) in a channel flow.

We would finally like to dwell into the details of the TT source term tensor and determine the relative importance of each factor. To do so, we follow the path of Kim (1989) and more recently of Hornung *et al.* (2019) and calculate the spatial derivative of the source

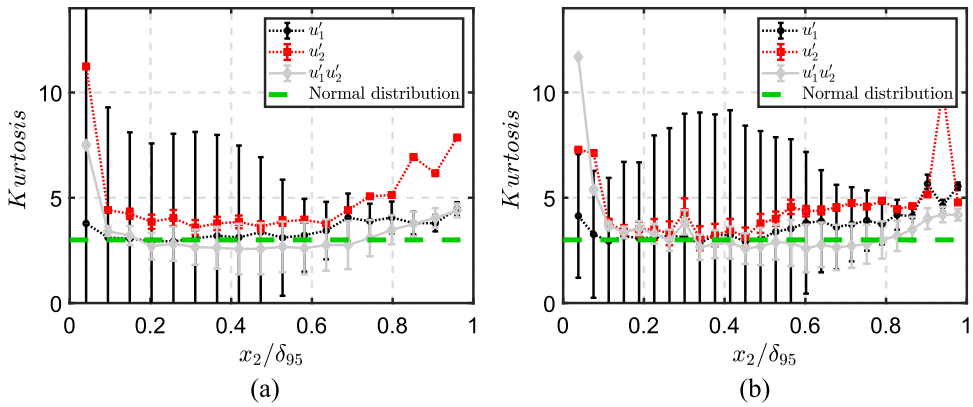

FIG. 21. Flatness factor. (a) x_1 = RMP 21 and (b) x_1 = RMP 26.

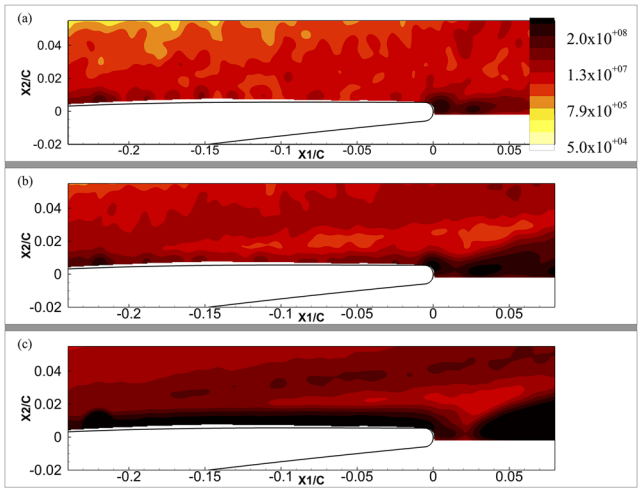

FIG. 22. The mean square source terms in a plane perpendicular to the airfoil. (a) $(\frac{du_1'}{dx_1})^2$, (b) $\frac{du_2'}{dx_1}\frac{du_1'}{dx_2}$, and (c) $(\frac{du_2'}{dx_2})^2$.

term to estimate the relative importance of each individual factor. The trailing edge noise has a dipole-type directivity, and its amplitude is highest perpendicular to the airfoil chord at the mid-span [see Brooks and Hodgson (1981), for instance]. Therefore, for such an observer location, the contribution to the far-field acoustic noise from the velocity fluctuations in the spanwise direction can then be ignored. Hence, the present study will only consider the factors comprising velocity disturbances in the wall-tangential and wall-normal directions. In Fig. 22, the spatial derivative of the wall-normal velocity fluctuations $(\frac{du_2'}{dx_2})^2$ is seen to be the strongest, followed by $\frac{du_2'}{dx_1}\frac{du_1'}{dx_2}$, and the weakest term is $(\frac{du_1'}{dx_1})^2$. The reason might be the relative homogeneity in the wall-parallel planes, as reported in Sec. V A. The fact that $(\frac{du_2'}{dx_2})^2$ is the highest contributor in our case differs from the results of the previous study of Hornung *et al.* (2019). The dominance of $(\frac{du_2'}{dx_2})^2$ is most likely caused by the fact that the turbulence is well established in our case and the flow seems to be statistically similar near the trailing edge [see Moreau and Roger (2005), for instance]. Thus, for the fourth objective, we can conclude that for a flow that behaves statistically similar near the trailing edge, the variation of the wall-normal velocity fluctuations is the dominant far-field noise generation term for an observer placed perpendicular to the airfoil.

The fourth-order two-point velocity correlation [see Eq. (10)] used to describe the source field of TT terms has been used in the past to describe jet noise. Therefore, the natural course of action is then to take advantage of several simplifications that have been previously made [see Morris and Zaman (2010), for instance]. The first simplification without making any assumption on the statistical distribution of velocity co-variance was proposed by Lighthill (1993) who showed that if the mean square velocity fluctuations and the flatness factor are independent of the separation distance, then the fourth-order two-point correlation is just the square of the second-order two-point velocity correlation. It must be noted however that Lighthill's simplification is valid only for the velocity fluctuations in the longitudinal direction. Figure 23 shows that Lighthill's approximation seems to capture the shape and the levels of the correlation $C_{22,22}$ well. This result is rather encouraging, and it is hoped that in the future, Lighthill's approximation can be extended in the transverse direction as well. For all modeling perspective, given that the second-order two-point velocity correlation is captured well with an exponential function, the fourth-order two-point velocity correlation can be successfully captured using a Gaussian function. In fact, the success of such a Gaussian fit for modeling $C_{ij,kl}$ has already been established by Karabasov *et al.* (2010) for the jet case.

VIII. EVALUATION OF THE WALL-PRESSURE SPECTRA

Having modeled the MS and TT source terms of Eq. (5) in Secs. VI and VII, respectively, their relative contribution to the wall pressure fluctuations p' can be finally assessed from Eqs. (8) and (9) in Sec. IV. For instance, the presumably dominant MS term comprises the mean shear, the wall-normal velocity fluctuations, and the two-point zero time-delay correlation of the wall-normal velocity [see Eq. (8)]. All this necessary information is only available above RMP 26, and the wall-pressure reconstruction is therefore limited to this location, which is anyway the only necessary input in Amiet's trailing-edge noise model. To prevent the limited

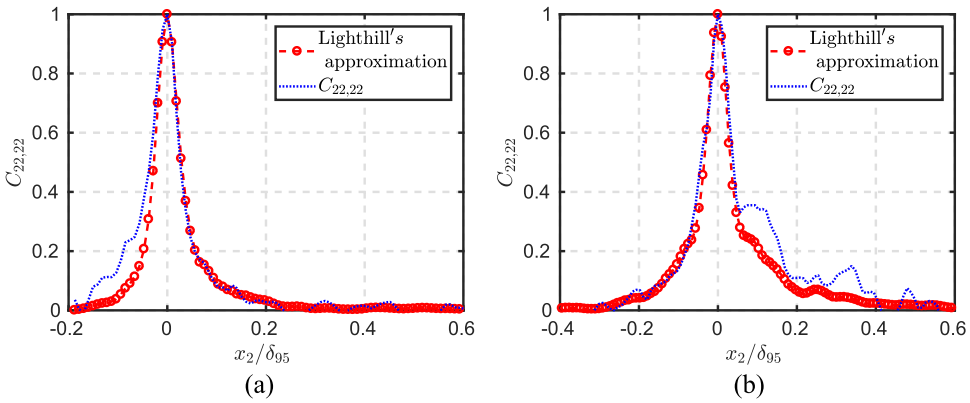

FIG. 23. Lighthill's approximation of the fourth-order two-point zero time–delay correlation at RMP 26 (a) at $x_2 = 0.2 \times \delta_{95}$ and (b) at $x_2 = 0.5 \times \delta_{95}$.

resolution and dynamic range inherent to any PIV system near the wall and its effect on pressure reconstruction, as detailed in the past by Ghaemi *et al.* (2012) and van Oudheusden (2013), the present experimental data have been supplemented by the near-wall values of anisotropy γ taken from the DNS of the same configuration by Wu *et al.* (2019) as already done previously by Grasso *et al.* (2019). The convection velocity is also assumed to be $0.72 \times U_\infty$, consistently with all previous measurements in different test facilities for the same flow configuration. Numerical evaluation of the MS and TT terms, which involve quintuple integrals, using quadrature methods is prohibitive. Therefore, Monte Carlo methods are used, the feasibility and robustness of which have been recently evaluated by Grasso *et al.* (2018). To facilitate the numerical implementation of the Monte Carlo scheme, Eqs. (8) and (9) are transformed into polar coordinates.

Furthermore, all the length scales within the integral are normalized by the boundary layer thickness. For the present study, the method of quasi-random sampling technique and importance sampling for the variance reduction has been used. The quasi-random sampling technique is known to improve the rate of convergence by a factor of $N^{-1/2}$ (where N is the number of samples) compared to when the Monte Carlo integration is done using a sequence of pseudo-random numbers [see p. 299 of Press *et al.* (1992)]. The quasi-random sequence is based on the Sobol sequence taken directly from Press *et al.* (1996). To further accelerate the rate of convergence, the method of importance sampling is used [as done in the past by Grasso *et al.* (2018), Linebarger (1972), Panton and Linebarger (1974), and Remmler *et al.* (2010)]. Although the method of importance sampling has been described in detail by Grasso *et al.* (2018), the main steps of the procedure are recalled for the sake of completeness.

The method of importance sampling is based on the simple idea that by introducing a change in a variable, the function could be made flatter in the new coordinate system, and hence, fewer samples would be required to reach convergence. Mathematically, the process of importance sampling amounts to solving the following equation:

$$E_f[h(Y)] = \int_Y h(\boldsymbol{X}) g(\boldsymbol{X}) \mathrm{d}\boldsymbol{X}. \tag{27}$$

In the above equation, the expectation E_f of function $h(\boldsymbol{X})$ is sought under the Probability Density Function (PDF) $g(\boldsymbol{X})$ in the domain Y. In the present case, $h(\boldsymbol{X})$ represents the integrand of Eq. (8), the integration of which is to be carried out. $\boldsymbol{X}$ stands for the five independent variables over which the integration is performed.

To solve the quintuple integral to evaluate Eq. (8), the choice of $g(\boldsymbol{X})$ has to be made for the leading terms in each of the independent variables X_i present in $h(\boldsymbol{X})$. The choice itself is dictated by step 1 of the algorithm. From there on, samples could be drawn from the function $g(\boldsymbol{X})$ using the technique known as inverse transform sampling.

The algorithm for inverse transform sampling can be summarized as follows:

(1) Determine the PDF function $g(X_i)$ that "resembles" $h(X_i)$.
(2) Determine its Cumulative Distribution Function (CDF) $u(X_i)$ from $g(X_i)$.
(3) Find its inverse $u^{-1}(X_i)$ either numerically or analytically.
(4) Generate uniformly distributed random numbers using the Sobol sequence and plug it to $u^{-1}(X_i)$, which generates a random number based on the PDF $g(X_i)$.
(5) Solve Eq. (27).

The first CDF is constructed for the variable k_3 and is exactly the one used by Linebarger (1972),

$$u(k_3) = \frac{k_1}{k^2 \tan^{-1}\left(\frac{b}{k_1}\right)}, \tag{28}$$

where b represents the upper limit of integration used for the wavenumber k_3. Subsequently, the CDF for the variables x_2, x_2', and r is chosen to be equal to

$$u(x_2) = \frac{\exp(-x_2)}{\exp(-a_1) - \exp(-a_2)}, \tag{29}$$

where a_1 and a_2 are the limits of integration for the variable. Finally, for the variance reduction in the polar angle θ, the following CDF has been used:

$$u(\theta) = \frac{1}{2 \times \sqrt{(\theta \times 2\pi)}}. \tag{30}$$

The wall-pressure spectra calculated are then expressed as a function of frequency under the hypothesis of frozen turbulence. The final wall-pressure spectra above RMP 26 are shown in Fig. 24. An integration over the frequency range 0.1 kHz–10 kHz yields p_{rms}. Its normalized value p_{rms}/τ_w of 9.4 is consistent with the distribution reported by Wang *et al.* (2009) on the same airfoil for the same flow condition. Compared with the wall-pressure spectra from a ZPG case as in Choi and Moin (1990), the low-frequency region has much higher levels contributing to the larger p_{rms}/τ_w. The latter is also larger than the value of 3.7 reported by Na and Moin (1998) as the present APG is more severe. Yet, when the rms of the wall pressure is normalized by the local maximum Reynolds shear stress, we

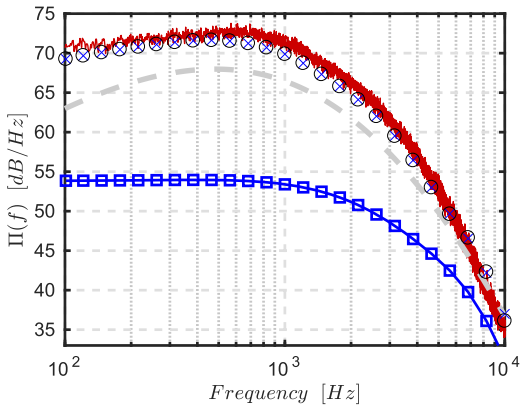

FIG. 24. Comparison of wall-pressure spectra models against experimental measurements at RMP 26. Legends: red solid curve—probe RMP 26; gray dashed curve—Rozenberg's model; black open circle—MS term quasi-random sampling; blue crosses—MS term importance sampling; and blue curve with open squares—$TT_{22,22}$ quasi-random sampling.

obtain about 2.7, which is consistent with the near plateau between 2.5 and 3 reported by Na and Moin (1998) and Abe (2017).

In Fig. 24, the MS term is seen to successfully capture the experimental levels and slopes. The so-called mid-frequency universal scaling, as well as the high-frequency roll-off, is well captured. Figure 24 also confirms that the variance reduction using either the importance sampling or the quasi-random sampling performs exceedingly well and differences are negligible at least on a dB scale. Rozenberg's model is unable to capture the correct levels at low frequencies. It is worth mentioning that for the input of Rozenberg's model boundary layer, integral parameters were calculated based on 99% of U_e, as proposed by Rozenberg *et al.* (2012). Finally, the most dominant in-plane TT term, $TT_{22,22}$, has been evaluated. For the range of frequency of interest, the contribution of the $TT_{22,22}$ term is negligible compared to the MS term for the wall-pressure spectra reconstruction. For far-field noise estimation for an observer placed perpendicular to the airfoil, just the contribution from the MS term would be enough. These conclusions thus answer the fourth objective of the paper.

As shown in the past [see Linebarger (1972) and Panton and Linebarger (1974), for instance], different regions of boundary layers contribute to different bands of frequencies for the wall-pressure spectra. This information is quite valuable since it can directly link the contribution to a particular band of frequencies to a specific layer within the boundary layer. To do this, first of all, we divide the boundary layer in three different regions:

(1) Inner-layer extending from the wall (IL) to $0.15 \times \delta_{95}$ (IU) $(0 \le x_2^+ < 33.3)$
(2) Middle-layer extending from $0.15 \times \delta_{95}$ (ML) to $0.45 \times \delta_{95}$ (MU) $(33.3 \le x_2^+ < 100)$
(3) Outer-layer extending from $0.45 \times \delta_{95}$ (OL) to δ_{95} (OU) $(100 \le x_2^+ < 220.5)$.

Subsequently, to identify regions of frequency that are generated by different layers, we subdivide integral I as

$$I = \iint_0^\infty \int_0^{2\pi} \Bigg[\int_{x_2^{IL}}^{x_2^{IU}} \int_{x_2'^{IL}}^{x_2'^{IU}} + 2 \int_{x_2^{IL}}^{x_2^{IU}} \int_{x_2'^{ML}}^{x_2'^{MU}} + 2 \int_{x_2^{IL}}^{x_2^{IU}} \int_{x_2'^{OL}}^{x_2'^{OU}} + \int_{x_2^{ML}}^{x_2^{MU}} \int_{x_2'^{ML}}^{x_2'^{MU}} + 2 \int_{x_2^{ML}}^{x_2^{MU}} \int_{x_2'^{OL}}^{x_2'^{OU}} + \int_{x_2^{OL}}^{x_2^{OU}} \int_{x_2'^{OL}}^{x_2'^{OU}} \mathrm{d}x_2 \mathrm{d}x_2' \Bigg] \times \mathrm{d}\theta \mathrm{d}k_3 \mathrm{d}r. \tag{31}$$

The above methodology was first used by Linebarger (1972) and Panton and Linebarger (1974) to identify regional contribution of the wall-pressure spectra. The results shown in Fig. 25 reinforce the claim that wall-pressure fluctuations are caused by nonlocal events, and as such, local scales based exclusively on either outer or inner parameters of the boundary layer are insufficient [see Camussi (2013), for instance]. This non-locality of pressure fluctuations is especially true at low frequencies where various regions contribute. The inner layer contributes the most to higher frequencies as expected because of the small scales involved. However, one key difference with Panton and Linebarger (1974) is that the present calculations do not show the "unexpected" changes in concavity (points where the second derivative is equal to zero) for the middle layer contribution. A distinct shift from the edge of the shear layer

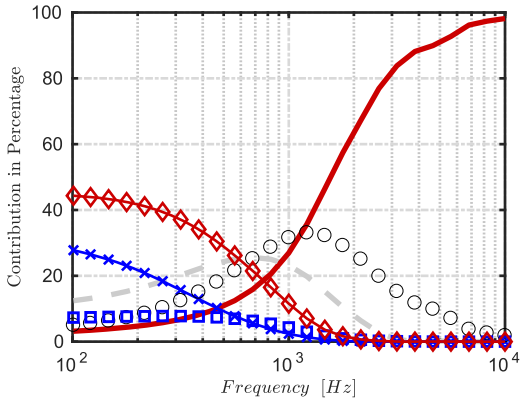

FIG. 25. Regional contribution of the MS term at RMP 26. Legends: red solid curve—inner layer; black open circles—inner–middle layer; blue open squares—inner–outer layer; gray dashed line—middle layer; red curve with open diamonds—middle-outer layer; and blue curve with crosses—outer layer.

TABLE V. Zonal distribution in percentage of the rms of the wall pressure.

Inner (IN)	Middle (MD)	Outer (OT)	IN-MD	IN-OT	MD-OT
30.3	18.1	6.4	22.8	4.6	17.8

to the near-wall region is observed with an increase in frequency. A quick drop from the contribution of the middle and outer layer terms is observed at high frequencies (starting from 3000 Hz). The low-frequency part is mostly dominated by the outer and middle parts of the boundary layer and their cross term, as also observed by Anantharamu and Mahesh (2020). The reason for such a behavior is most likely caused by the local severe adverse pressure gradient, which results in the presence of large coherent structures nearer the wall [see Panton and Linebarger (1974), for instance]. The inner–outer part contributes the least (as expected) to the wall-pressure spectrum due to the significant separation distance between these layers, which results in a loss of correlation (R_{22}). Its contribution is only significant at low frequencies (below 1000 Hz), and its contribution at higher frequencies reduces quickly to almost zero. The high-frequency contributions therefore come from stratified regions within the boundary layer and not because of global motions, as already suggested by Blake (2017). By again integrating over frequencies each contribution in Eq. (31), similar conclusions can be drawn on p_{rms}, as shown in Table V.

IX. CONCLUSION

A comprehensive approach to wall-pressure spectrum modeling in the wavenumber domain based on Poisson's equation has been presented and tested for the attached turbulent flow past the CD airfoil at 8° and a Reynolds number of 1.5×10^5 (based on the chord length and inlet velocity), for which a significant adverse pressure gradient exists at the trailing edge. The models proposed

for the individual source terms, i.e., the MS and TT terms, show that the velocity correlation is very important for the wall-pressure spectra.

The present study confirms the existence of very large structures for wall-tangential fluctuations in the outer parts of the boundary layer, the size of which is typically 1.5–2 δ_{95}. In any plane parallel to the wall, both wall-tangential and normal velocity correlation profiles are homogeneous. The existence of flow homogeneity is quintessential in allowing simplifications to be made in the wall-pressure modeling [see Blake (2017), Grasso *et al.* (2019), Panton and Linebarger (1974), and Remmler *et al.* (2010), for instance]. In contrast, in the plane perpendicular to the wall, the correlation contours of the wall-normal velocity correlation are anisotropic and inhomogeneous. The inhomogeneity is caused by the blocking of the wall that stops the development of the turbulent structures. The assumption of homogeneous turbulence in the wall-normal direction is bound to give erroneous results as shown when a homogeneous model such as EAM [proposed by Slama *et al.* (2018)] is used. Furthermore, toward the wall, the correlation profile is found to collapse, giving rise to self-similarity when normalized by the upper point, as first shown by Hunt *et al.* (1987). The blocking effect is likely responsible for the compression of the correlation isocontours close to the wall. However, increasing the mean pressure gradient seems to counteract the effect of blocking, thus rendering self-similarity less noticeable. In short, the effect of the pressure gradient opposes blocking of the eddies by the wall. Generally, the effect of the pressure gradient decreases the correlation in the velocity profiles. Therefore, with increasing pressure gradient, the structure becomes less and less correlated within the boundary layer away from the wall. Although the adverse pressure gradient, mean-shear, and blocking appear to be competing, their relative importance varies across the wall-tangential and wall-normal directions. Close to the wall, blocking is found to dominate, especially when the moving point of the two-point wall-normal velocity correlation moves in the direction of the wall. The importance of blocking near the wall becomes more evident when considering the correlation length Λ_{22}^{2-} that collapses irrespective of the pressure gradient near the wall (~40%).

Because of the competing effects of blocking, pressure gradient, and wall shear, modeling of the wall-normal velocity is difficult using isotropic turbulence models. However, slightly away from the wall and especially in the wall-tangential direction, the exponential function is found to properly capture the correlation decay. The isotropic turbulence model can then be used with a fair degree of success, provided that the two-point correlation length is a function of both the moving and the fixed point. For the wall-normal velocity correlation, the transverse correlation length is almost half of the longitudinal correlation length, which is intrinsic to isotropic models. Mixing-length theory provides one way of estimating it. However, the effect of blocking should be incorporated, and therefore, the model of Hunt and Morrison (2000) provides a more reasonable path.

A new model is proposed to quantify the contribution to the wall-pressure spectra of the TT term that requires estimation of fourth-order statistics, making it challenging to evaluate. The alternative route of using the normal distribution hypothesis of Millionshchikov (1941) to reduce the complexity has been pursued in the past [see Grasso *et al.* (2019), Hodgson (1962), and Slama *et al.* (2018), for instance]. However, the current experimental study and several other studies [see Chang (1998), Kim (1989), and Srinath (2017), for instance] have shown that the normal distribution does not apply close to the wall in particular, even though the relative uncertainty in the fourth-order statistics of the experimental data presented in the present study is high. An alternative estimation of the fourth-order statistics using second-order statistics, which is mathematically rigorous and does not invoke the assumption of the normal distribution of the fourth-order statistics, has been proposed by Lighthill (1993). Such an estimate seems to agree well with the current PIV data. Another difficulty lies in the fact that the TT shear noise term requires determination of a fourth-order tensor, and even though some of the terms are symmetric and equal, the number of terms to be modeled remains comparatively large. The present experiment confirms that the wall-normal term TT_{22} is larger than the source terms TT_{11} and TT_{12}, consistently with the homogeneity of turbulence in any plane parallel to the wall. Therefore, for an observer placed in the mid-span location and perpendicular to the airfoil chord, the MS and TT_{22} terms contribute the most to the perceived airfoil self-noise. However, estimation of the pressure spectra shows that the MS term contribution is substantially higher than that of the TT_{22} term.

Moreover, good agreement between the measured wall-pressure and the reconstructed MS term is found. Therefore, the methodology proposed in the current paper provides a novel way to reconstruct wall-pressure spectra using a low-repetition rate PIV system without using elaborate numerical schemes to solve for pressure. Another advantage of such an approach is that it allows unraveling the regional contributions toward the total wall-pressure spectra within the boundary-layer for a given frequency. The regional contribution of the MS term suggests that the near-wall region mostly governs high-frequency contribution ($x_2^+ < 33.3$). Low-frequency contribution is mostly governed by the middle and outer layers. Furthermore, a clear transition when approaching the wall is observed with an increase in frequency, and consequently, no point of inflexion for the contribution of any given layer is found, which is contrast to the findings of Panton and Linebarger (1974). It is hoped that by linking velocity field statistics to wall-pressure, latter information can be used to improve the existing semi-empirical models and develop novel noise reduction techniques using flow control strategies.

ACKNOWLEDGMENTS

P.J. would like to acknowledge the help and support of colleagues Marlene Sanjosé and Thomas Léonard for processing initial sets of the planar-PIV data. The authors equally acknowledge the generous supervision of Professor Fulvio Scarano during both experimental campaigns. Last but not least, the help of S. Orestano is gratefully acknowledged for providing anisotropy data and checking wall-pressure spectra calculations. The authors gratefully acknowledge the support of the Canadian NSERC Discovery Grant (No. RGPIN-2014-04111).

APPENDIX: MODELING OF THE TT INTERACTION SOURCE TERM

The starting point is the solution of Poisson's equation, retaining only the TT factor as a source term, in the wavenumber space as

pursued by Kraichnan (1956) and recalled recently by Grasso *et al.* (2019), for instance. Here, we start with the solution of Eq. (5) with the boundary conditions given by Eqs. (6) and (7).

Equation (5) is Fourier transformed in a plane parallel to the wall. The following equation is then obtained:

$$\frac{\partial^2 \hat{p}}{\partial x_1 \partial x_1} + \frac{\partial^2 \hat{p}}{\partial x_2 \partial x_2} + \frac{\partial^2 \hat{p}}{\partial x_3 \partial x_3} = -\hat{T}(\mathbf{K}, x_2). \tag{A1}$$

Here, $(\hat{X})$ denotes the spatial Fourier transform of a variable X. The source term in Eq. (A1) is $\hat{T}_{ij}(\mathbf{K}, x_2') = \frac{\partial^2 \hat{T}T_{ij}}{\partial x_i \partial x_j}$. The TT term is itself a second-order velocity tensor, and the summation of its individual components comprises the complete source field. They have been listed in Table VI for completeness. Equation (A1) is a second-order non-homogeneous ordinary differential equation, the solution of which can be obtained using a standard procedure, as shown in the past by Linebarger (1972) and more recently by Grasso *et al.* (2019). The final solution can be written as

$$\hat{p}(\mathbf{K}, 0) = \frac{\rho}{k} \int_0^\infty e^{(-kx_2')} \hat{T}_{ij}(\mathbf{K}, x_2') \mathrm{d}x_2'. \tag{A2}$$

To take the Fourier transform of individual terms, we make use of the following four properties of the Fourier transform:

$$\hat{f}^n(k) = (ik)^n f(\hat{k}),$$

$$\left[\hat{fg}\right](\mathbf{k}) = \int_{\mathbb{K}^m} \hat{f}(\mathbf{k} - \mathbf{k}')\, \hat{g}(\mathbf{k}')\, \mathrm{d}\mathbf{k}', \tag{A3}$$

$$\partial \frac{[f(x)^* g(x)]}{\partial x} = \frac{\partial f(x)}{\partial x}^* g(x), \tag{A4}$$

$$[a\hat{f} + b\hat{g}] = a\hat{f} + b\hat{g}. \tag{A5}$$

The final tensor T_{ij} is simplified with the abovementioned properties and by the use of integration by parts. To obtain the autospectra, Eq. (A2) is multiplied by its complex conjugate. Taking the ensemble average, we have

$$\overline{\hat{p}(\mathbf{k}, 0)\hat{p}^*(\mathbf{k}', 0)} = \frac{\rho^2}{kk'} \iint_0^\infty \overline{e^{(-kx_2')} \hat{T}_{ij}(\mathbf{k}, x_2') e^{(-k'x_2)} \hat{T}_{ij}^*(\mathbf{k}', x_2)} \mathrm{d}x_2 \mathrm{d}x_2'. \tag{A6}$$

TABLE VI. Decomposition of the TT tensor.

$\hat{TT}_{11} = \frac{\partial^2 (\hat{u_1'u_1'} - \overline{u_1'u_1'})}{\partial {x_1}^2}$	$\hat{TT}_{12} = \frac{\partial^2 (\hat{u_1'u_2'} - \overline{u_1'u_2'})}{\partial x_1 \partial x_2}$	$\hat{TT}_{13} = \frac{\partial^2 (\hat{u_1'u_3'} - \overline{u_1'u_3'})}{\partial x_1 \partial x_3}$
$\hat{TT}_{21} = \hat{TT}_{12}$	$\hat{TT}_{22} = \frac{\partial^2 (\hat{u_2'u_2'} - \overline{u_2'u_2'})}{\partial {x_2}^2}$	$\hat{TT}_{23} = \frac{\partial^2 (\hat{u_2'u_3'} - \overline{u_2'u_3'})}{\partial x_2 \partial x_3}$
$\hat{TT}_{31} = \hat{TT}_{13}$	$\hat{TT}_{32} = \hat{TT}_{23}$	$\hat{TT}_{33} = \frac{\partial^2 (\hat{u_3'u_3'} - \overline{u_3'u_3'})}{\partial {x_3}^2}$

TABLE VII. Simplified version of the TT source term.

$\hat{T}_{11} = -{k_1}^2[\hat{TT}_{11}]$	$\hat{T}_{12} = ik_1 k[\hat{TT}_{12}]$	$\hat{T}_{13} = -k_1 k_3[\hat{TT}_{13}]$
$\hat{T}_{21} = \hat{T}_{12}$	$\hat{T}_{22} = k^2[\hat{TT}_{22}]$	$\hat{T}_{23} = ik_3 k[\hat{TT}_{23}]$
$\hat{T}_{31} = \hat{T}_{13}$	$\hat{T}_{32} = \hat{T}_{23}$	$\hat{T}_{33} = -{k_3}^2[\hat{TT}_{33}]$

Since the flow is homogeneous in the wall-tangential direction, we can simplify Eq. (A6) using the following two identities:

$$\overline{\hat{p}(\mathbf{k}, 0) \times \hat{p}^*(\mathbf{k}', 0)} = \Pi(0, \mathbf{k}) \delta(\mathbf{k} - \mathbf{k}') \mathrm{d}\mathbf{k} \mathrm{d}\mathbf{k}', \tag{A7}$$

$$\overline{\hat{T}_{ij}(k, x_2) \times \hat{T}_{ij}^*(k', x_2')} = \phi_{ij,kl}(x_2, x_2', \mathbf{k}) \delta(\mathbf{K} - \mathbf{k}') \mathrm{d}\mathbf{k} \mathrm{d}\mathbf{k}'. \tag{A8}$$

The final expression for the wall spectra caused by the TT interaction term is thus given by the following equation:

$$\Pi(0, \mathbf{K}) = \frac{\rho^2}{k^2} \iint_0^\infty \phi_{ij,lm}(x_2, x_2', \mathbf{K}) e^{-K(x_2 + x_2')} \mathrm{d}x_2 \mathrm{d}x_2'. \tag{A9}$$

It is worth mentioning that Eq. (A9) together with the source terms described in Table VII is almost the same as found by Chase (1980). To see this more clearly, we divide the source terms in Table VII by k^2 and multiply Eq. (A9) by k^4. The final expression for the wavenumber spectra can then be written as

$$\Pi(0, \mathbf{K}) = \rho^2 k^2 \iint_0^\infty S_{ij,lm}(x_2, x_2', \mathbf{K}) e^{-K(x_2 + x_2')} \mathrm{d}x_2 \mathrm{d}x_2'. \tag{A10}$$

The source terms are now also given by [see Chase (1980), for instance]

$$\hat{T}_s = \frac{\left[-\left({k_1}^2 \hat{TT}_{11} + 2k_1 k_3 \hat{TT}_{13} + {k_3}^2 \hat{TT}_{33}\right) + i2k\left(k_1 \hat{TT}_{12} + k_3 \hat{TT}_{32}\right) + k^2 \hat{TT}_{22}\right]}{k^2}. \tag{A11}$$

This is not at all surprising since both approaches after all solve the same set of equations. Yet, we do find two notable differences that come from the methodology used to obtain the source term. The first one is rather trivial in that Eq. (A10) describes the wall pressure spectra solely in the wavenumber domain. In contrast, Chase's model gives the wall-pressure spectra in the wavenumber–frequency domain. This is due to the fact that we have just spatially Fourier-transformed the source term, whereas Chase (1980) applied

a spatio-temporal transformation to it. The second difference is that we retain the mean operator in the source term tensor $\hat{T}_{ij}$. To see this more clearly, we write out the source term explicitly,

$$\hat{TT}_{ij}(\mathbf{K},x_2) = \int \Big(\hat{u}_i(\mathbf{K}',x_2)\hat{u}_j(\mathbf{K}-\mathbf{K}',x_2) - \overline{\hat{u}_i(\mathbf{K}',x_2)\hat{u}_j(\mathbf{K}-\mathbf{K}',x_2)}\Big)\mathrm{d}^2\mathbf{K}'. \tag{A12}$$

Following Chase (1980), if we define a source $\tilde{T}_{ij}$ as $\hat{T}\hat{T}_{ij}$ but with 3 axis taken along **K**, the source term can be reduced to

$$\hat{T}_s = -\tilde{T}_{33} + i2\tilde{T}_{32} + \tilde{T}_{22}. \tag{A13}$$

Finally, the corresponding cross-power wavenumber spectra can be written as

$$\hat{S}_{ij,lm}(\mathbf{K},x_2,x_2') = \int \overline{\Big(\hat{u}_i(\mathbf{K}',x_2')\hat{u}_j(\mathbf{K}-\mathbf{K}',x_2') - \overline{\hat{u}_i(\mathbf{K}',x_2')\hat{u}_j(\mathbf{K}-\mathbf{K}',x_2')}\Big)}\,\overline{\Big(\hat{u}_l(\mathbf{K}',x_2)\hat{u}_m(\mathbf{K}-\mathbf{K}',x_2) - \overline{\hat{u}_l(\mathbf{K}',x_2)\hat{u}_m(\mathbf{K}-\mathbf{K}',x_2)}\Big)}\mathrm{d}^2\mathbf{K}'. \tag{A14}$$

One can also describe the cross-power wavenumber spectra as just the spatial Fourier transform of the two-point velocity correlation of the fourth order at zero time delay in a plane parallel to the wall and is given by

$$\hat{S}_{ij,lm}(\mathbf{k},x_2,x_2') = \frac{[u_i\bar{u}_j - \overline{u_i\bar{u}_j}](x_2)[u_i\bar{u}_j - \overline{u_i\bar{u}_j}](x_2')}{4\pi^2} \times \int C_{ij,lm}(r_1,x_2,x_2',r_3)e^{-i(\mathbf{k}\cdot\mathbf{r})}\mathrm{d}^2\mathbf{r}', \tag{A15}$$

where $\mathbf{r}_{1,3} = (r_1, r_3)$ and $[u_i\bar{u}_j - \overline{u_i\bar{u}_j}](x_2) = \sqrt{\overline{(u_iu_j - \overline{u_iu_j})^2}(x_2)}$. For the sake of clarity, it can be recalled that the fourth-order two-point velocity zero time delay correlation is given by Eq. (10) in Sec. IV B. Equation (A15) can be re-written as a function of the wall-tangential wavenumber by integrating Eq. (A12) in k_3 and substituting in Eq. (A15),

$$\Pi(k_1) = \frac{\rho^2}{4\pi^2}\int_0^\infty\iiint_{-\infty}^{\infty}\Big[k^2\mathrm{e}^{(-k(x_2+x_2'))} \times C_{ij,lm}(r_1,x_2,x_2',r_3)[u_i\bar{u}_j - \overline{u_i\bar{u}_j}](x_2)[u_i\bar{u}_j - \overline{u_i\bar{u}_j}] \times (x_2')\mathrm{e}^{-i(k_1r_1+k_3r_3)}\Big]\mathrm{d}r_3\mathrm{d}r_1\mathrm{d}k_3\mathrm{d}x_2\mathrm{d}x_2'. \tag{A16}$$

Finally, taking advantage of the symmetry in the variables r_1, r_3, and k_3, Eq. (A16) can be simplified to

$$\Pi(k_1) = \frac{2\rho^2}{\pi^2}\int_0^\infty\Big[k^2\, e^{-k(x_2+x_2')}\, C_{ij,lm}(r_1,x_2,x_2',r_3) \times [u_i\bar{u}_j - \overline{u_i\bar{u}_j}](x_2)[u_i\bar{u}_j - \overline{u_i\bar{u}_j}](x_2')\, e^{-i(k_1r_1+k_3r_3)}\Big] \times \mathrm{d}r_1\mathrm{d}r_3\mathrm{d}k_3\mathrm{d}x_2\mathrm{d}x_2'. \tag{A17}$$

DATA AVAILABILITY

Raw data were generated at the Delft University of Technology's large scale facility. The data that support the findings of this study are available from the corresponding author upon reasonable request.

REFERENCES

Abe, H., "Reynolds-number dependence of wall-pressure fluctuations in a pressure-induced turbulent separation bubble," J. Fluid Mech. **833**, 563–598 (2017).

Abe, H., "Direct numerical simulation of a turbulent boundary layer with separation and reattachment over a range of Reynolds numbers," Fluid Dyn. Res. **51**, 011409–011424 (2019).

Abe, H., Matsuo, Y., and Kawamura, H., "A DNS study of Reynolds-number dependence on pressure fluctuations in a turbulent channel flow," in *4th International Symposium on Turbulence and Shear Engineering* (Katholieke Universiteit Leuven, 2005).

Adrian, L., Adrian, R. J., and Westerweel, J., *Particle Image Velocimetry* (Cambridge University Press, 2011), p. 30.

Ahmadi, F., Ebrahimian, M., Sanders, R. S., and Ghaemi, S., "Particle image and tracking velocimetry of solid–liquid turbulence in a horizontal channel flow," Int. J. Multiphase Flow **112**, 83–99 (2019).

Albarracin, C., Doolan, C., Jones, R., Hansen, C., Brooks, L., and Teubner, M. D., "A RANS-based statistical noise model for trailing edge noise," AIAA Paper No. 2012-2181, 2012.

Amiet, R. K., "Noise due to turbulent flow past a trailing edge," J. Sound Vib. **47**, 387–393 (1976).

Anantharamu, S. and Mahesh, K., "Analysis of wall-pressure fluctuation sources from direct numerical simulation of turbulent channel flow," J. Fluid Mech. **898**, A17:1–A17:36 (2020).

Atkinson, C. and Soria, J., "An efficient simultaneous reconstruction technique for tomographic particle image velocimetry," Exp. Fluids **47**, 553 (2009).

Batchelor, G. K., *The Theory of Homogeneous Turbulence* (Cambridge University Press, 1953).

Bendat, J. S. and Piersol, A. G., *Random Data: Analysis and Measurement Procedures* (John Wiley & Sons, 2011), p. 729.

Benedict, L. H. and Gould, R. D., "Towards better uncertainty estimates for turbulence statistics," Exp. Fluids **22**, 129–136 (1996).

Blake, W. K., *Mechanics of Flow-Induced Sound and Vibration*, Complex Flow-Structure Interactions Vol. 2 (Academic Press, 2017).

Boukharfane, R., Bodart, J., Jacob, M. C., Joly, L., Bridel-Bertomeu, T., and Node-Langlois, T., "Characterization of the pressure fluctuations within a controlled-diffusion airfoil boundary layer at large Reynolds numbers," AIAA Paper No. 2019-2722, 2019.

Brooks, T. F. and Hodgson, T. H., "Trailing edge noise prediction from measured surface pressures," J. Sound Vib. **78**, 69–117 (1981).

Camussi, R., *Noise Sources in Turbulent Shear Flows: Fundamentals and Applications* (Springer Science & Business Media, 2013), Vol. 545.

Chang III, P. A., "Relationships between turbulent wall pressure and velocity field sources," Ph.D. thesis, University of Maryland, 1998.

Chase, D. M., "Modeling the wavevector-frequency spectrum of turbulent boundary layer wall pressure," J. Sound Vib. **70**, 29–67 (1980).
Choi, H. and Moin, P., "On the space-time characteristics of wall-pressure fluctuations," Phys. Fluids A **2**, 1450–1460 (1990).
Christophe, J. and Moreau, S., "LES of the trailing-edge flow and noise of a controlled-diffusion airfoil at high angle of attack," in *Proceedings of the 2008 Summer Program* (Center for Turbulence Research, Stanford University, 2008), pp. 305–316.
Christophe, J., Moreau, S., Hamman, C., Witteveen, J. A. S., and Iaccarino, G., "Uncertainty quantification for the trailing-edge noise of a controlled-diffusion airfoil," AIAA J. **53**, 42–54 (2015).
Clauser, F. H., "The turbulent boundary layer," in *Advances in Applied Mechanics* (Elsevier, 1956), Vol. 4, pp. 1–51.
Coles, D., "The law of the wake in the turbulent boundary layer," J. Fluid Mech. **1**, 191–226 (1956).
De-Kat, R. and Van-Oudheusden, B. W., "Instantaneous planar pressure determination from PIV in turbulent flow," Exp. Fluids **52**, 1089–1106 (2012).
De La Riva, D. H., Devenport, W. J., Muthanna, C., and Glegg, S. A. L., "Behavior of turbulence flowing through a compressor cascade," AIAA J. **42**, 1302–1313 (2004).
Foucaut, J. M., Carlier, J., and Stanislas, M., "PIV optimization for the study of turbulent flow using spectral analysis," Meas. Sci. Technol. **15**, 1046 (2004).
Gavin, J. R., "Unsteady forces and sound caused by boundary layer turbulence entering a turbomachinery rotor," Ph.D. thesis, The Pennsylvania State University, 2002.
Ghaemi, S., "Pressure fluctuations in the turbulent boundary layer; advances in diagnostics and control," Ph.D. thesis, Delft University of Technology, 2013.
Ghaemi, S., Ragni, D., and Scarano, F., "PIV-based pressure fluctuations in the turbulent boundary layer," Exp. Fluids **53**, 1823–1840 (2012).
Glegg, S. and Devenport, W. J., *Aeroacoustics of Low Mach Number Flow: Fundamentals, Analysis and Measurement* (Academic Press Elsevier, 2007).
Grant, H. L., "The large eddies of turbulent motion," J. Fluid Mech. **4**, 149–190 (1958).
Grasso, G., Jaiswal, P., and Moreau, S., "Monte-Carlo computation of wall-pressure spectra under turbulent boundary layers for trailing-edge noise prediction," in *International Conference on Noise and Vibration Engineering* (Katholieke Universiteit Leuven, 2018).
Grasso, G., Jaiswal, P., Wu, H., Moreau, S., and Roger, M., "Analytical models of the wall-pressure spectrum under a turbulent boundary layer with adverse pressure gradient," J. Fluid Mech. **877**, 1007–1062 (2019).
Gravante, S. P., Naguib, A. M., Wark, C. E., and Nagib, H. M., "Characterization of the pressure fluctuations under a fully developed turbulent boundary layer," AIAA J. **36**, 1808–1816 (1998).
Gungor, A. G., Maciel, Y., Simens, M. P., and Soria, J., "Analysis of a turbulent boundary layer subjected to a strong adverse pressure gradient," J. Phys.: Conf. Ser. **506**, 012007–012014 (2014).
Hinze, J. O., *Turbulence—An Introduction to its Mechanism and Theory* (McGraw-Hill College, 1975).
Hodgson, T. H., "Pressure fluctuations in shear flow turbulence," Ph.D. thesis, University of London, 1962.
Hornung, C., Lutz, T., and Krämer, E., "A model to include turbulence-turbulence interaction in the prediction of trailing edge far field noise for high angles of attack or slightly separated flow," Renewable Energy **136**, 945–954 (2019).
Hu, N., "Empirical model of wall pressure spectra in adverse pressure gradients," AIAA J. **56**, 3491–3506 (2018).
Hunt, J. C. R., "A theory of turbulent flow round two-dimensional bluff bodies," J. Fluid Mech. **61**, 625–706 (1973).
Hunt, J. C. R. and Graham, J. M. R., "Free-stream turbulence near plane boundaries," J. Fluid Mech. **84**, 209–235 (1978).
Hunt, J. C. R., Moin, P., Lee, M., Moser, R. D., Spalart, P., Mansour, N. N., Kaimal, J. C., and Gaynor, E., "Cross correlation and length scales in turbulent flows near surfaces," in *Advances in Turbulence* (Springer, 1989), Vol. 2, pp. 128–134.
Hunt, J. C. R., Moin, P., Moser, R. D., and Spalart, P. R., "Self similarity of two point correlations in wall bounded turbulent flows," in *Proceedings of the 1987 Summer Program* (Center for Turbulence Research, Stanford University, 1987), pp. 25–36.
Hunt, J. C. R. and Morrison, J. F., "Eddy structure in turbulent boundary layers," Eur. J. Mech., B: Fluids **19**, 673–694 (2000).
Kamruzzaman, M., Lutz, T., Kraemer, E., and Wuerz, W., "On the length scales of turbulence for aeroacoustic applications," AIAA Paper No. 2011-2734, 2011.
Karabasov, S. A., Afsar, M. Z., Hynes, T. P., Dowling, A. P., McMullan, W. A., Pokora, C. D., Page, G. J., and McGuirk, J. J., "Jet noise: Acoustic analogy informed by large eddy simulation," AIAA J. **48**, 1312–1325 (2010).
Kim, J., "On the structure of pressure fluctuations in simulated turbulent channel flow," J. Fluid Mech. **205**, 421–451 (1989).
Kraichnan, R. H., "Pressure fluctuations in turbulent flow over a flat plate," J. Acoust. Soc. Am. **28**, 378–390 (1956).
Krogstad, P. and Skåre, P., "Influence of a strong adverse pressure gradient on the turbulent structure in a boundary layer," Phys. Fluids **7**, 2014–2024 (1995).
Lee, M. J. and Hunt, J. C. R., "The structure of sheared turbulence near a plane boundary," in *Turbulent Shear Flows* (Springer, 1991), Vol. 7, pp. 101–118.
Lee, S., "Empirical wall-pressure spectral modeling for zero and adverse pressure gradient flows," AIAA J. **56**, 1818–1829 (2018).
Liepmann, H. W., Laufer, J., and Liepmann, K., "On the spectrum of isotropic turbulence," Technical Report No. 2473, National Advisory Committee for Aeronautics, 1951.
Lighthill, M. J., "An estimate of the covariance of TXX without using statistical assumptions," in *Computational Aeroacoustics*, edited by Hardin, J. C. and Hussaini, M. Y. (Springer-Verlag, 1993).
Linebarger, J. H., "Computation of the spectra of turbulent boundary layer surface-pressure fluctuations," Ph.D. thesis, Oklahoma State University, 1972.
Mahinder, S. U., "Quadruple velocity correlations and pressure fluctuations in isotropic turbulence," J. Aeronaut. Sci. **20**, 197–204 (1953).
McAuliffe, B. R. and Yaras, M. I., "Transition mechanisms in separation bubbles under low- and elevated-freestream turbulence," J. Turbomach. **132**, 011004 (2010).
Millionshchikov, M. D., "On the theory of homogeneous isotropic turbulence," Dokl. Akad. Nauk SSSR **32-9**, 615–618 (1941).
Monty, J. P., Harun, Z., and Marusic, I., "A parametric study of adverse pressure gradient turbulent boundary layers," Int. J. Heat Fluid Flow **32**, 575–585 (2011).
Moreau, S., Henner, M., Iaccarino, G., Wang, M., and Roger, M., "Analysis of flow conditions in freejet experiments for studying airfoil self-noise," AIAA J. **41**, 1895–1905 (2003).
Moreau, S., Laffay, P., Idier, A., and Atalla, N., "Several noise control of the trailing-edge noise of a controlled-diffusion airfoil," AIAA Paper No. 2016-2816, 2016.
Moreau, S., Neal, D., and Foss, J., "Hot-wire measurements around a controlled-diffusion airfoil in an open-jet anechoic wind tunnel," J. Fluids Eng. **128**, 699–706 (2006).
Moreau, S. and Roger, M., "Effect of airfoil aerodynamic loading on trailing edge noise sources," AIAA J. **43**, 41–52 (2005).
Moreau, S. and Roger, M., "Back-scattering correction and further extensions of Amiet's trailing-edge noise model. Part II: Application," J. Sound Vib. **323**, 397–425 (2009).
Morilhat, S., Chedevergne, F., and Simon, F., "A unified methodology to evaluate the radiated noise due to turbulent boundary layer flows," J. Fluids Eng. **141**, 061201 (2019).
Morris, P. J. and Zaman, K. B. M. Q., "Velocity measurements in jets with application to noise source modeling," J. Sound Vib. **329**, 394–414 (2010).
Na, Y. and Moin, P., "The structure of wall-pressure fluctuations in turbulent boundary layers with adverse pressure gradient and separation," J. Fluid Mech. **377**, 347–373 (1998).
Neal, D. R., "The effects of rotation on the flow field over a controlled-diffusion airfoil," Ph.D. thesis, Michigan State University, 2010.
Oberlack, M., "A unified approach for symmetries in plane parallel turbulent shear flows," J. Fluid Mech. **427**, 299–328 (2001).
Panton, R. L. and Linebarger, J. H., "Wall pressure spectra calculations for equilibrium boundary layers," J. Fluid Mech. **65**, 261–287 (1974).

Parchen, R., "Progress report draw: A prediction scheme for trailing-edge noise based on detailed boundary layer characteristics," Technical Report No. HAG-RPT-980023, TNO Institute of Applied Physics, The Outhouse Netherlands, 1998.

Perot, B. and Moin, P., "Shear-free turbulent boundary layers. Part 1: Physical insights into near-wall turbulence," J. Fluid Mech. **295**, 199–227 (1995).

Press, W. H., Teukolsky, S. A., Vetterling, W. T., and Flannery, B. P., *Numerical Recipes in Fortran* (Press Syndicate of the University of Cambridge, New York, NY, 1992), Vol. 1, p. 77.

Press, W. H., Teukolsky, S. A., Vetterling, W. T., and Flannery, B. P., *Numerical Recipes in Fortran* (Cambridge University Press, Cambridge, 1996), Vol. 2, p. 90.

Ragni, D., Avallone, F., van der Velden, W. C. P., and Casalino, D., "Measurements of near-wall pressure fluctuations for trailing-edge serrations and slits," Exp. Fluids **60**, 6 (2019).

Remmler, S., Christophe, J., Anthoine, J., and Moreau, S., "Computation of wall pressure spectra from steady flow data for noise prediction," AIAA J. **48**, 1997–2007 (2010).

Roger, M. and Moreau, S., "Broadband self noise from loaded fan blades," AIAA J. **42**, 536–544 (2004).

Roger, M. and Moreau, S., "Back-scattering correction and further extensions of Amiet's trailing-edge noise model. Part 1: Theory," J. Sound Vib. **286**, 477–506 (2005).

Rozenberg, Y., Robert, G., and Moreau, S., "Wall-pressure spectral model including the adverse pressure gradient effects," AIAA J. **50**, 2168–2179 (2012).

Sandberg, R. D. and Jones, L. E., "Direct numerical simulations of low Reynolds number flow over airfoils with trailing-edge serrations," J. Sound Vib. **330**, 3818–3831 (2011).

Sanjosé, M., Moreau, S., Kim, M. S., and Pérot, F., "Direct self-noise simulation of the installed controlled diffusion airfoil," AIAA Paper No. 2011-2716, 2011.

Schneiders, J. F. G., Avallone, F., Pröbsting, S., Ragni, D., and Scarano, F., "Pressure spectra from single-snapshot tomographic PIV," Exp. Fluids **59**, 57 (2018).

Sillero, J. A., Jiménez, J., and Moser, R. D., "Two-point statistics for turbulent boundary layers and channels at Reynolds numbers up to $\delta^+ = 2000$," Phys. Fluids **26**, 105109 (2014).

Slama, M., Leblond, C., and Sagaut, P., "A Kriging-based elliptic extended anisotropic model for the turbulent boundary layer wall pressure spectrum," J. Fluid Mech. **840**, 25–55 (2018).

Srinath, S., "Modeling and prediction of near wall turbulent flows," Ph.D. thesis, École centrale de Lille, 2017.

Stalnov, O., Chaitanya, P., and Joseph, P. F., "Towards a non-empirical trailing edge noise prediction model," J. Sound Vib. **372**, 50–68 (2016).

Stewart, R. W., "Triple velocity correlations in isotropic turbulence," in *Mathematical Proceedings of the Cambridge Philosophical Society* (Cambridge University Press, 1951), Vol. 47, pp. 146–157.

Thomas, N. H. and Hancock, P. E., "Grid turbulence near a moving wall," J. Fluid Mech. **82**, 481–496 (1977).

Townsend, A. A. R., *The Structure of Turbulent Shear Flow* (Cambridge University Press, 1980).

van Oudheusden, B. W., "PIV-based pressure measurement," Meas. Sci. Technol. **24**, 032001 (2013).

von Kármán, T., "Progress in the statistical theory of turbulence," Proc. Natl. Acad. Sci. U. S. A. **34**, 530–539 (1948).

Wang, M., Moreau, S., Iaccarino, G., and Roger, M., "LES prediction of wall-pressure fluctuations and noise of a low-speed airfoil," Int. J. Aeroacoust. **8**, 177–197 (2009).

Westerweel, J. and Scarano, F., "Universal outlier detection for PIV data," Exp. Fluids **39**, 1096–1100 (2005).

Wilson, D. K., "Three-dimensional correlation and spectral functions for turbulent velocities in homogeneous and surface-blocked boundary layers," Technical Report No. ARL-TR-1287, Army Research Lab, Adelphi, MD, 1997.

Winkler, J. and Moreau, S., "LES of the trailing-edge flow and noise of a NACA6512-63 airfoil at zero angle of attack," in *Proceedings of the 2008 Summer Program* (Center for Turbulence Research, Stanford University, 2008), pp. 331–342.

Wu, H., Moreau, S., and Sandberg, R. D., "Effects of pressure gradient on the evolution of velocity-gradient tensor invariant dynamics on a controlled-diffusion aerofoil at $Re_c = 150\,000$," J. Fluid Mech. **868**, 584–610 (2019).

Wu, H., Sanjosé, M., Moreau, S., and Sandberg, R. D., "Direct numerical simulation of the self-noise radiated by the installed controlled-diffusion airfoil at transitional Reynolds number," AIAA Paper No. 2018-3797, 2018.

Zawadzki, I., Gershfield, J. L., Na, Y., and Wang, M., "Hydroacoustic forcing function modeling using DNS database," in *Proceedings of the 1996 Summer Program* (Center for Turbulence Research, Stanford University, 1996), pp. 369–384.